TECHNISCHE
UNIVERSITÄT
WIEN
Vienna University of Technology

# DIPLOMARBEIT

# Ilmenite and mixtures with Olivine as oxygen carriers in a chemical looping combustion pilot plant

**Ausgeführt am Institut für**

**Verfahrenstechnik, Umwelttechnik und Technische Biowissenschaften**

**der Technischen Universität Wien**

**unter der Anleitung von Univ.Prof. Dr. Hermann Hofbauer und**

**Dr. Tobias Pröll**

**durch**

**Karl Mayer**

**0025285**

**Augasse 14, 2471 Pachfurth**

2. September 2010

# Danksagung

An erster Stelle möchte ich mich bei Herrn Univ.Prof. Dr. Hermann Hofbauer für die Ermöglichung dieser Arbeit bedanken.

Mein Dank gilt auch Dr. Johannes Bolhàr-Nordenkampf, Dr. Phillip Kolbitsch und Dr. Tobias Pröll für die Betreuung und Unterstützung bei der Erstellung der Arbeit.

Ein weiterer Dank ist an alle Kollegen der Arbeitsgruppe Zukunftsfähige Energietechnik zu richten, für das sehr inspirierende und angenehme Klima.

Besonderer Dank gilt meiner Familie und besonders meinen Eltern, die mir dieses Studium mit viel Geduld und Verständnis ermöglichten.

Ich möchte mich aber ganz besonders bei Dir, liebe Monika, bedanken für die vielen geopferten Stunden, das Verständnis und die Motivation die du mir zukommen hast lassen.

# Abstract

Chemical looping combustion (CLC) has been identified as key technology for carbon capture and storage (CCS) with inherent $CO_2$-separation. A solid oxygen carrier is used to supply the oxygen for fuel oxidation. This process is realised in two fluidized bed reactors. The air-reactor, which is operated as a fast fluidized riser, is used to oxidise the oxygen carrier. The oxygen carrier is reduced by the fuel in the fuel-reactor, which is operated in bubbling or turbulent fluidization regime. The bed material, which is the oxygen carrier, circulates between air-reactor and fuel-reactor.

In this work a dual circulating fluidized bed (DCFB) reactor system has been used to investigate the CLC process for operation with natural minerals as oxygen carrier. Pure ilmenite, a mixture of ilmenite with olivine and a mixture of ilmenite with a Ni-enriched olivine are the bed materials used in this work. A sample gas preparation unit is designed to dry the filtered sample gas streams to a dew point of 4 °C to protect the online gas analysers. During hot operation solids samples are taken from the upper loop seal. Five samples from the hot unit, two from the filter box, four after the experiments and fresh material are analysed using X-ray diffraction (XRD) analysis to characterize the composition of the particles. A sample of fresh ilmenite and a solids sample from the hot unit are analysed using a thermogravimetric analysis (TGA) to describe the reduction and the oxidation process of the material. TGA- and XRD-results are used to identify the reactions taking place in both reactors. Ilmenite reacts to pseudobrookite and rutile in the air-reactor which is reduced to ilmenite in the fuel-reactor.

An oxidative thermal pretreatment program has been established to avoid agglomerations of ilmenite during CLC operation.

The results of eleven experiments are used to characterize the CLC-process with different natural minerals as bed materials. During the experiments the fuel load in the fuel-reactor is varied from $20\,kW$ to $120\,kW$. The fuels used are: natural gas, a model syngas and $H_2$ diluted with $N_2$. To identify a possible dependency on the gas-solid contact time the solids inventory of the rig is varied from $70\,kg$ to $85\,kg$. It is possible to define an active solids inventory, using the pressure drop over the fluidized bed. This active solids inventory changes with changing fluidization of the reactors. Since this change has an effect on the gas-solid contact time the active solids inventory is monitored during the experiments. A temperature variation is done with natural gas and $H_2$ at constant fuel load in the fuel-reactor. Fuel conversion is low using methane as fuel and ilmenite as bed material. Conversion is better when using a model syngas as fuel but full conversion is not reached.

The addition of olivine has little effect on methane conversion, the slight positive effect observed could also be the result of the increase of bed inventory. The addition of Ni-olivine has little effect on conversion, it is even lower than with natural olivine. Using ilmenite, methane and hydrogen conversions are getting better with increasing temperature.
Based on the results of this work, ilmenite is not a good bed material for methane as fuel. Using syngas as fuel, e.g. from gasification of coal or other solid fuels, and a higher process temperature, ilmenite can be advantageous compared to artificial particles as oxygen carrier. In such a process ash has to be removed from the bed which causes also a loss of bed material. Since artificial particles are much more expensive than ilmenite solid fuels CLC will likely be realisable only with the cheap and easy to handle natural bed material. Furthermore reactions of the bed material with the ash could harm the reactivity and the catalytic activity of the material. Especially the performance of designed particles with defined surfaces could be negatively affected from the presence of ash. Ilmenite fulfils these demands and can be considered as a good candidate for chemical looping combustion of solid fuels.

# Kurzfassung

Chemical Looping Combustion (CLC) wurde als Schlüsseltechnologie für Carbon Capture and Storage (CCS) mit inhärenter $CO_2$-Abtrennung identifiziert. Ein Feststoff dient als Sauerstoffträger, der Sauerstoff für die Verbrennung bereitstellt. Das Verfahren ist in zwei Wirbelschichtreaktoren ausgeführt. Der Luft-Reaktor, er wird als schnell fluidisierter Riser betrieben, dient zur Oxidation des Sauerstoffträgers. Der Sauerstoffträger wird im Brennstoff-Reaktor durch den Brennstoff reduziert. Der Brennstoff-Reaktor wird als blasenbildende oder turbulente Wirbelschicht betrieben. Das Bettmaterial, welches als Sauerstoffträger dient, zirkuliert zwischen den beiden Reaktoren.

In dieser Arbeit wurde ein Dual Circulating Fluidized Bed (DCFB) Reaktorsystem verwendet um den CLC-Prozess zu untersuchen. Besonderes Augenmerk wurde auf die Verwendung von natürlichen Mineralien als Sauerstoffträger gelegt. Reiner Ilmenit, eine Mischung aus Ilmenit und Olivin und eine Mischung aus Ilmenit und einem Nickel-imprägnierten Olivin dienten als Bettmaterial. Eine Messgasaufbereitung wurde entworfen und gebaut, welche die bereits gefilterten Messgasströme bis zu einem Taupunkt von 4 °C trocknet und die Online-Messgeräte vor kondensierendem Wasser schützt. Während des Betriebs der Versuchsanlage wurden Feststoffproben aus dem oberen Siphon genommen. Insgesamt wurden fünf Proben aus der heißen Anlage, zwei aus der Filterbox, vier nach den Versuchen und eine vom frischen Material gezogen und mittels Röntgendiffraktometrie (XRD) analysiert. Eine Probe des frischen Materials und eine Probe aus der heißen Anlage wurden auch mit einer thermogravimetrischen Analyse (TGA) untersucht um die Reduktion und die Oxidation des Bettmaterials zu untersuchen. Die Ergebnisse der TGA und XRD Untersuchungen dienten dazu, die Reaktionen in den Reaktoren zu erklären. Ilmenit reagiert zu Pseudobrookit und Rutil im Luft-Reaktor und wird im Brennstoff-Reaktor zu Ilmenit reduziert.

Um Agglomerationen von Ilmenit im CLC-Betrieb zu vermeiden wurde eine thermische Vorbehandlung von frischem Material unter oxidierenden Bedingungen eingeführt. Die Ergebnisse aus elf Experimenten werden verwendet um den CLC-Prozess mit natürlichen Mineralien als Bettmaterial zu beschreiben. In den Experimenten werden Lastvariationen des Brennstoffs von 20 $kW$ bis 120 $kW$ durchgeführt. Als Brennstoff dienen Erdgas, ein Modellsynthesegas und $H_2$ verdünnt mit $N_2$. Um eine mögliche Abhängigkeit von der Gas-Feststoff-Kontaktzeit zu erkennen wird das Gesamtbettinventar der Anlage zwischen 70 $kg$ und 85 $kg$ variiert. Es kann ein aktives Bettinventar definiert werden, indem man den Druckverlust über das Bett zur Berechnung heranzieht. Dieses aktive Bettinventar ändert sich mit der Fluidisierung der Reaktoren was zu einer Änderung der Gas-Feststoff-Kontaktzeit führt. Daher wird auch das aktive Bettinventar und dessen Änderungen beobachtet. Eine Temperaturvariation wird mit Erdgas und $H_2$ bei konstanter Last durchgeführt. Der Brennstoffumsatz ist gering bei der Verwendung von Methan als Brennstoff. Bei der Verwendung des Modellsynthesegases wird ein besserer Umsatz erzielt aber vollständige Umsetzung des Brennstoffs wird nicht erreicht. Die Zugabe von Olivin hat nur einen geringen Effekt auf den Brennstoffumsatz. Die Verbesserung kann auch durch die Erhöhung des Bettmaterialinventars hervorgerufen werden. Die Zugabe von Ni-Olivin hat ebenfalls einen geringen Effekt auf den Umsatz, er ist sogar geringer als durch Zugabe von natürlichem Olivin. Allgemein zeigt sich bei Verwendung von Ilmenit eine Verbesserung sowohl des Methan- als auch des Wasserstoffumsatzes bei Temperaturerhöhung.

Basierend auf den Ergebnissen dieser Arbeit zeigt sich, dass Ilmenit, bei Verwendung von Methan als Brennstoff, nicht der ideale Sauerstoffträger für CLC ist. Bei der Verwendung von Synthesegas, z.B. aus der Vergasung von Kohle oder anderen festen Brennstoffen und bei höheren Prozesstemperaturen kann die Verwendung von Ilmenit Vorteile gegenüber der Verwendung von künstlich hergestellten Sauerstoffträgern bringen. In solchen Prozessen muss der anfallende Aschestrom entfernt werden, dies führt auch zu einem Verlust von Bettmaterial. Da künstlich hergestellte Sauerstoffträgerpartikel sehr viel teurer sind als Ilmenit kann solch ein Prozess nur mit dem billigen und einfach handhabbaren natürlichen Material realisiert werden. Weiters können Reaktionen der Asche mit dem Bettmaterial dessen Reaktivität und katalytische Aktivität herabsetzen. Besonders bei den synthetisch hergestellten Partikeln kann dies zu einer Einbuße der Reaktivität führen. Ilmenit erfüllt die Anforderungen für Festbrennstoff-CLC und kann als vielversprechender Kandidat für die Rolle des Sauerstoffträgers gehandelt werden.

# Contents

# 1. Introduction

## 1.1. The greenhouse effect and greenhouse gas emissions

Global warming is an effect which should not be neglected any more. The effects and dangers are already visible and influence the lives of many people. Arctic ice is melting, the ocean levels are rising, extreme weather phenomena are more likely. These are only some of the effects of climate change. According to the Intergovernmental Panel on Climate Change (IPCC) the average temperature increased in the $20^{th}$ century from about 13.3 °C to 14.5 °C. As shown in Figure 1.1, not only average temperature is rising, also the global average sea level climbed for about $5\,cm$ in the last 40 years of the last century. As a consequence of the global warming the average snow cover of the Northern Hemisphere is decreasing in the last decades. The IPCC has its own definition for climate change:

> *Climate change in IPCC usage refers to a change in the state of the climate that can be identified (e.g. using statistical tests) by changes in the mean and/or the variability of its properties, and that persists for an extended period, typically decades or longer. It refers to any change in climate over time, whether due to natural variability or as a result of human activity.* [1]

A lot of substances have been identified as greenhouse gases (GHG). To compare them, although they have different radiative properties and lifetimes in the atmosphere the carbon dioxide equivalent ($CO_2 - eq$) emission and the $CO_2 - eq$ concentration have been defined, based on the radiative forcing of $CO_2$.

- $CO_2 - eq$ **emission** is the amount of $CO_2$ emission that would cause the same time integrated radiative forcing, over a given time period, as an emitted amount of a long lived greenhouse gas. The equivalent $CO_2$ emission is obtained by multiplying the emission of the greenhouse gas by its greenhouse warming potential for the given time period.
- $CO_2 - eq$ **concentration** is the concentration of $CO_2$ that would cause the same amount of radiative forcing as a given mixture of $CO_2$ and other green house gases.

According to this definition the global warming potential of $CO_2$ is 1. Other common greenhouse gases from power generation using fossile fuels are methane

($CH_4$) and nitrous oxide ($N_2O$). For a time horizon of 100 years the global warming potential of these two substances is 21 for methane and 310 for nitrous oxide [2].

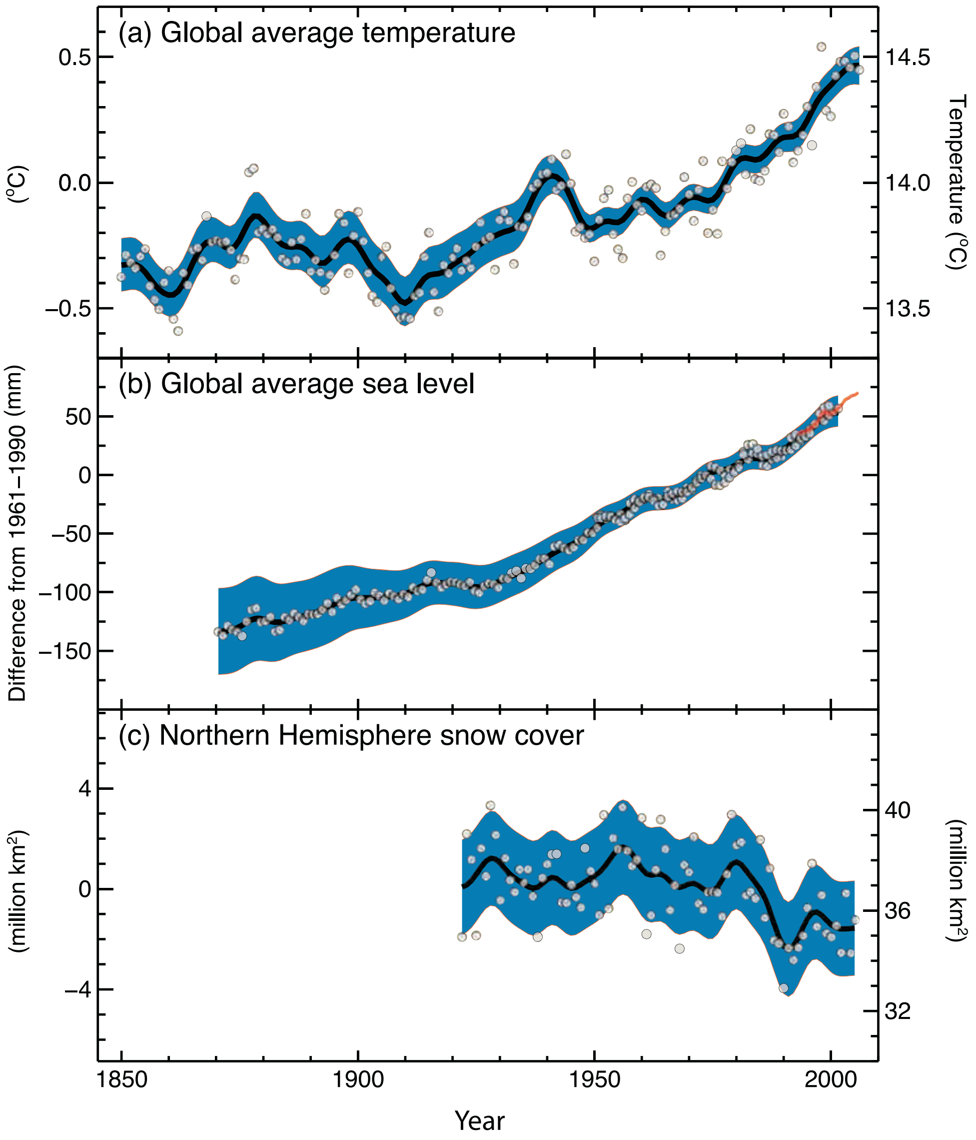

Figure 1.1.: Observed changes in global average temperature, global average sea level and Northern Hemisphere snow cover for March to April. [1]

The radiative forcing values of the greenhouse gases $CO_2$, $CH_4$, $N_2O$, halocarbons, ozone and also for aerosols are shown in Figure 1.2. In the last column also the level of scientific understanding (LOSU) of these effects is shown.

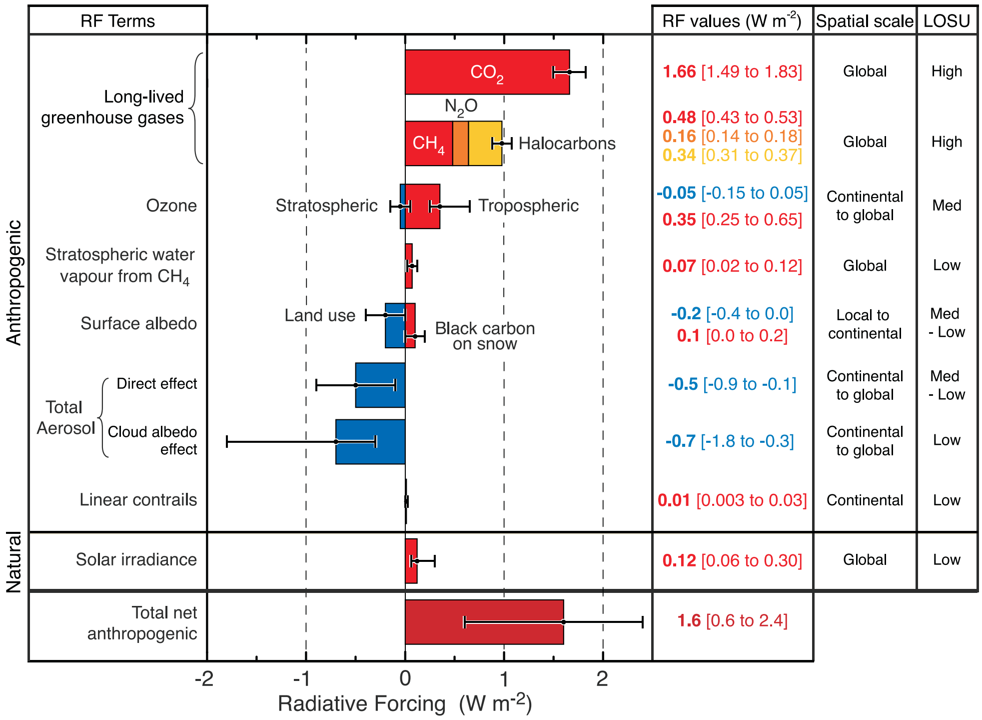

Figure 1.2.: Global mean radiative forcings (RF)in 2005 with their 90% confidence intervals for various agents and mechanisms. [2]

To reduce global warming a reduction of greenhouse gas emissions is necessary. To achieve this goal many options are possible. The increase of conversion efficiency allows equal electricity production with lower energy input. Another way to reduce GHG emissions is to substitute fossil fuels with renewable fuels such as biomass. Also an increase of renewable technologies will reduce GHG emissions, but this technology has its limitations. Hydro power is well developed and further expansion is limited. The use of wind energy is rapidly increasing and a large potential lies in offshore wind parks. Nuclear energy is, like biomass, a $CO_2$ free energy source but terms of long-time storage of nuclear waste are not solved and also uranium sources are limited. Another way to reduce $CO_2$ emissions is the optimization of energy saving, like the reduction of stand-by energy consumption of electronic devices and also their overall energy efficiency. Minimization of heat losses of buildings could decrease their energy consumption. Another step to reduce GHG emissions, especially $CO_2$, is carbon capture and storage (CCS). It allows the utilization of fossil fuels without the emission of $CO_2$ to the atmosphere. CCS is explained in detail in Section 1.2. Figure 1.3 shows two scenarios for the growth of carbon emissions until 2030. The 450 Policy scenario leads to a stabilization of greenhouse gases at $450 ppm\ CO_2-eq$ and the 550 Policy scenario leads to $550 ppm$.

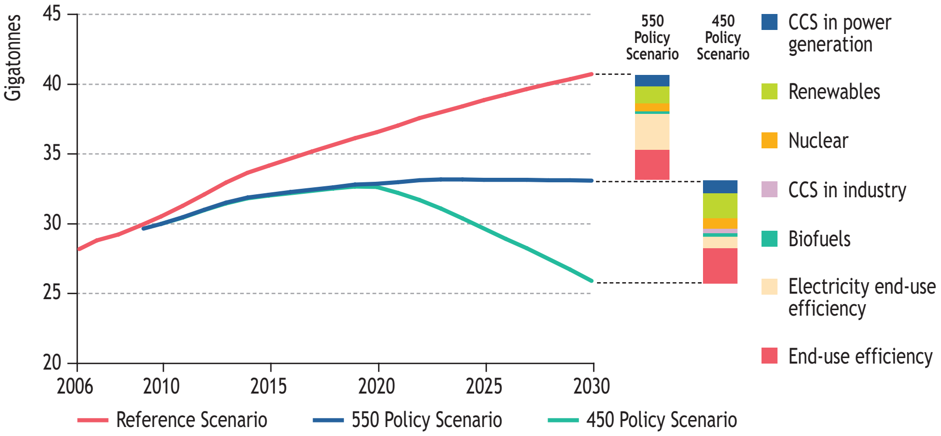

Figure 1.3.: Energy related $CO_2$ emissions by source in the 550 and 450 Policy Scenarios relative to the reference scenario [3]

## 1.2. Carbon Capture and Storage

To capture emitted carbon, a pure $CO_2$ stream has to be generated. In small scale applications like transportation and the building sector it would be difficult to separate carbon emissions. $CO_2$ separation makes sense in large scale units with a huge amount of carbon emissions focused in one point. The energy supply sector and industry fulfil this condition. For power plants, there are four possible ways to capture $CO_2$: post-combustion capture, pre-combustion capture, oxy-fuel combustion and unmixed combustion.

- post-combustion capture: This method is ideal for retrofitting existing units. An additional unit has to be installed to separate the $CO_2$. Due to the high content of nitrogen in the flue gas, amine scrubbers are applied to deal with the low $CO_2$ concentrations. The $CO_2$ separation unit has to be very large as a consequence of the high amount of flue gas in such power plants.
- pre-combustion capture: This is an available technology since many years. In production of synthesis gas the fuel is converted to syngas ($CO$ and $H_2$) from gasification of solid fuels or reforming of gaseous and liquid fuels. After a water-gas shift stage, almost all carbon is oxidized to $CO_2$ which can be separated from the $H_2$ easily.
- oxy-fuel combustion: The fuel is burnt with pure oxygen and recirculated flue gas. The flue gas mainly consists of $H_2O$ and $CO_2$ which is easy to separate from the steam. Air separation has to be done, which lowers the energy efficiency of the plant. A benefit of this way of combustion is the reduction of $NO_x$ emissions due to the lack of nitrogen in the combustor.

- unmixed combustion: Fuel and air are not mixed during combustion in this process. Oxygen is selectively transported from one reaction zone to another, where fuel is oxidized. Two off gas streams are generated, one consisting of depleted air (mostly $N_2$ with some excess $O_2$) and the other consisting of the oxidized fuel ($CO_2$ and $H_2O$). Solid oxide fuel cells (SOFC) and chemical looping combustion (CLC) use this concept. CLC is a potent candidate to make CCS possible without a high energy penalty for $CO_2$ separation.

The separated $CO_2$ has to be transported and stored. Transport will be done in pipelines for onshore transport and tankers will be used for transport to offshore storage facilities. Underground geological storage and ocean storage are the proposed ends of the $CO_2$ stream. To store $CO_2$ in geological formations it is trapped as gas or supercritical fluid covered from a layer of low permeability rock. $CO_2$ can also react with minerals and organic material and will become a part of the mineral matrix. $CO_2$ sequestration is already used to enhance oil recovery, the gas is injected into the oil reservoir to improve the mobility of the oil, causing an increase of productivity of the reservoir. Nowadays the $CO_2$ used for enhanced oil recovery is from natural sources. Changing to captured $CO_2$ will be an important step into reduction of GHG during oil production.

The storage of liquid $CO_2$ in the ocean in depths where the density of the $CO_2$ is higher than the sea water (3000m) shows a high storage potential, but has the biggest uncertainty of possible influences to the aquatic life and the sea bed too. A second way to store $CO_2$ in the ocean is to dissolve it in the sea water. This mechanism already takes place on the surface of the oceans.

According to a study carried out by The Boston Consulting Group (BGC) [4], CCS is a feasible, cost effective near term solution to eliminate a considerable portion of global carbon emissions. But the implementation in the near future will need subsidies, since the $CO_2$ price will not be high enough to make these projects profitable in the near term but after 2030 the price for $CO_2$ certificates will overcome the price for CCS.

## 1.3. Chemical looping combustion/reforming

The main part of chemical looping is the solids loop. It enables selective mass transport of a reactive species, in case of chemical looping combustion the oxygen transport from the air-reactor to the fuel-reactor (Figure 1.4). For chemical looping combustion two reaction zones are needed. One to oxidise the bed material, to start the oxygen transport, another to reduce the bed material again and to make the oxygen available for combustion. These two reaction zones are represented in the air-reactor, to oxidise the solids and the fuel-reactor to burn the fuel. The main advantage of this set-up is the separation of the air-stream and the fuel-stream. Using conventional combustion, the air is mixed with the fuel

and burned, the exhaust gas consists of the combustion products ($CO_2$, $H_2O$) and the nitrogen amount, brought in from the air. For $CO_2$ separation the nitrogen and also the steam have to be separated. Using chemical looping combustion, two exhaust gas streams exist. The off-gas from the air-reactor, which consists of nitrogen and some residual oxygen. The fuel-reactor off-gas mainly consists of steam and carbon dioxide. To separate the $CO_2$, only the steam has to be condensed and a pure stream of $CO_2$ is obtained. Overall, chemical looping combustion features inherent $CO_2$ separation, without the needs of special gas treatment.
It is possible to define a global stoichiometric air/fuel ratio in the CLC system. It represents the oxygen available in the air-reactor relating to the oxygen needed for full combustion of the fuel in the fuel-reactor. In chemical looping combustion the global air/fuel ratio is bigger than one. Reducing this value below one leads to operating conditions called chemical looping reforming (CLR). In CLR too little oxygen is available for combustion of the fuel. This leads to a $CO$ and $H_2$ rich product gas in the fuel-reactor, since reforming of the fuel takes place.

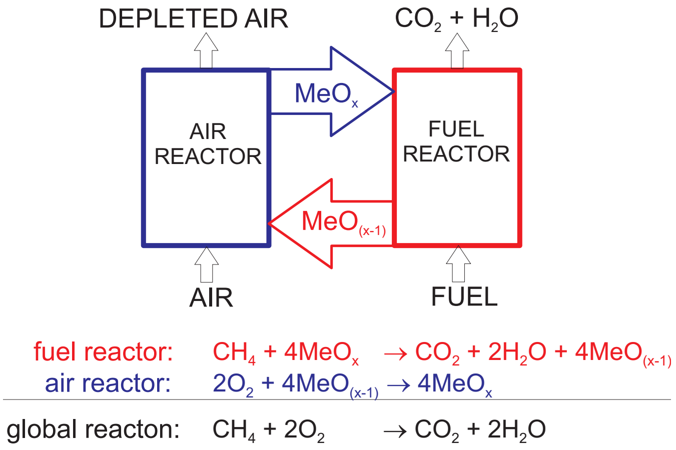

Figure 1.4.: scheme of chemical looping combustion

### 1.3.1. Air-reactor

The bed material which is reduced in the fuel-reactor has to be re-oxidized, to start another cycle of oxygen transport to the fuel-reactor. This regenerative step happens in the air-reactor. The main reaction is the oxidation of the metal or metal oxide in the bed material to a higher degree of oxidation. In case of nickel based oxygen carriers (compare [5]) metallic nickel is oxidised. When using the natural mineral ilmenite for oxygen transport iron and iron oxide are possible oxygen carriers. According to Abad [6] the generalized reaction in the air-reactor is:

$$Me_xO_{y-1} + {}^{1}\!/_{2}O_2 \rightarrow Me_xO_y \tag{1.1}$$

### 1.3.2. Fuel-reactor

The main requirement of the fuel-reactor is the conversion of the fuel. The fuel should fully react with the oxygen, transported from the bed material, to $CO_2$ and $H_2O$. The solids do not need to be fully reduced when leaving the fuel reactor, because the focus lies on the oxygen transport and full conversion of the fuel and not on full conversion of particle reduction in the fuel-reactor. Oxygen transport can be easily increased with increasing solids circulation. In this work the focus lies on methane and syngas as fuels. For chemical looping combustion in general also higher hydrocarbons and solid fuels, like coal, are possible feedstocks. According to Abad [6] the overall reaction in the fuel-reactor for a generalized metal oxide as bed material and a hydrocarbon as fuel, is:

$$(2n+m)Me_xO_y + C_nH_{2m} \rightarrow (2n+m)Me_xO_{y-1} + nCO_2 + mH_2O \qquad (1.2)$$

If syngas is used as fuel the reaction changes to:

$$(n+m)Me_xO_y + nCO + mH_2 \rightarrow (n+m)Me_xO_{y-1} + nCO_2 + mH_2O \qquad (1.3)$$

## 1.4. Oxygen carriers for chemical looping combustion

The most important issue to get convenient performance of chemical looping combustion is the reactivity of the bed material (the oxygen carrier). Many materials have been identified as potential oxygen carriers for chemical looping, e.g.: $CuO$, $NiO$, $Mn_3O_4$, $Fe_2O_3$ and $CoO$ [7] [5].

First investigations showed a high potential of $Cu$, $Fe$ and $Ni$ - based materials to fulfil the demands on oxygen transport capability, stability and reactivity. The materials used by Abad [5] are synthesised from pure chemicals. An inert alumina oxide core is impregnated with the oxygen carrier material to generate a particle with high porosity, low abrasion and good thermal stability. According to Abad all three materials show high reactivity, so they are valid to be used in chemical looping combustion.

Corbella [8] investigated the reactivity of titania-supported iron particles and the changes in phase chemistry. He found out that during reduction an ilmenite containing phase is built and reactivity is lower than that of $Ni$- and $Cu$- based materials. However, $Fe$- based particles are cheaper than others.

Ishida [9] investigated the effect of different production methods, sol-gel method and dissolution method, of particles containing $NiO$ on YSZ (yttria-stabilized zirconia)

Also mixing of oxygen carrier materials has been done. Johansson [10] mixed $Ni$- and $Fe$- particles, both with $MgAl_2O_4$ support, and compared the reactivity of the mixture to that of the pure substances. He found a synergetic effect, improving the fuel conversion.

The designed oxygen carriers show good performance, but they are expensive. They are interesting materials for chemical looping combustion using gaseous fuels, whereas cheap natural minerals have the potential to fulfil the requirements for solid fuel CLC. In this process ash has to be removed which leads to a loss of bed material too.

Ilmenite has been identified as such a potential bed material for chemical looping. It is a natural mineral with almost pure deposits. The price of the material is, compared with all the other oxygen carriers mentioned, extremely low.

### 1.4.1. Ilmenite [11] [12]

Ilmenite is a titanium-iron oxide mineral. Its color is iron-black or steel-grey. Ilmenite crystallizes in the trigonal system, like corundum ($Al_2O_3$) and hematite ($Fe_2O_3$)which have the same crystal structure. Natural ilmenite is never pure $FeTiO_3$. It is able to form solid solutions with geikielite ($MgTiO_3$) and pyrophanite ($MnTiO_3$), so contamination with manganese and magnesium is possible. Although, most of the natural deposits show a composition, close to pure ilmenite. At high temperatures miscibility with hematite and ulvospinel ($Fe_2^{2+}TiO_4$) exists. Beyond 950 °C ilmenite and ulvospinel show no miscibility gap.

Figure 1.5.: Picture of ilmenite sand

### 1.4.2. Olivine [12]

Olivine is a magnesium-iron silicate mineral. The color of this mineral is olive-green. The crystal system of olivine is orthorhombic. The amount of magnesium and iron varies in the range of the solid solution series. Forsterite ($Mg_2SiO_4$) is the Mg - endmember and fayalite ($Fe_2SiO_4$) the Fe - endmember. The generalized formula for olivine is: $(Mg, Fe)_2SiO_4$.

Figure 1.6.: Olivine; Credit: R.Weller, Cochise College

## 1.5. Scope of the work

Chemical looping combustion is a very attractive way to burn fossil fuels with the focus on CCS. In this work a 120kW chemical looping combustor was used to do a bechmark test for two natural minerals with focus on the usability of these materials as oxygen carrier for chemical looping combustion and fuel conversion. The rig is designed as a dual circulating fluidized bed reactor system (DCFB) [13], containing an air-reactor and a fuel-reactor. The main focus in this work lies on the mineral ilmenite, an iron and titanium containing oxide ($FeTiO_3$). It has been identified as a cheap and readily available oxygen carrier for chemical looping combustion. Ilmenite is not injurious to health, so it is easy to handle the bed material without special safety equipment. Also the disposal of used bed material is not problematic because it is not harmful to the environment. The conventional use of ilmenite is the production of $TiO_2$ pigments. During the purifying processes also some oxidation and reduction of the ilmenite takes place.

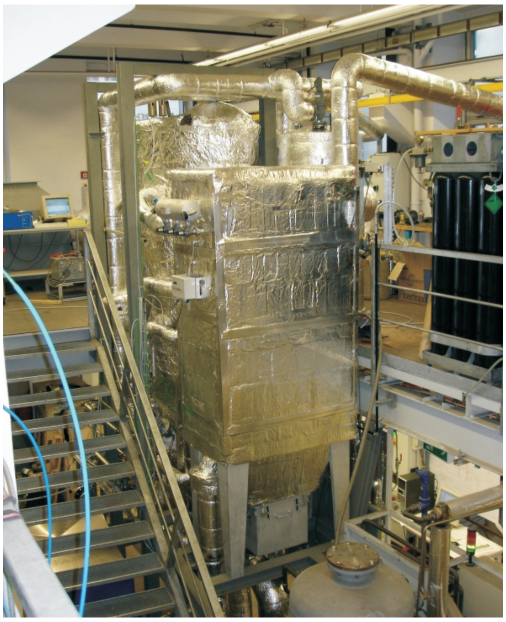

Figure 1.7.: picture of the chemical looping combustion unit

Olivine, a iron magnesium silicate ($(FeMg)2SiO4$), is the second bed material tested. This mineral is used as bed material in fluidized bed biomass gasification. According to Pfeifer et al. [14] olivine shows a moderate catalytic activity towards hydrocarbon reforming. In this work natural olivine and a nickel impregnated olivine are used as additives to ilmenite with respect to the improvement of the conversion of hydrocarbons.

# 2. Theoretical background

## 2.1. Chemical looping combustion

The CLC process has already been explained in Section 1.3, but only with generalized reaction equations. In the following sections the chemistry of ilmenite and the characteristic reactions that take place in CLC using ilmenite are described.

### 2.1.1. Ilmenite as oxygen carrier in chemical looping combustion

The name Ilmenite refers to the mineral $FeTiO_3$, but it is also used for $FeTiO_3$ rich minerals containing impurities of $MnO$, $MgO$ , $Fe2O3$ or $Ti_2O_3$ in the crystal structure [15]. Ilmenite is one of the most common minerals containing titanium [16]. Ilmenite, leucoxene (altered ilmenite) and rutile are the only titanium containing minerals with commercial importance. Ilmenite is recovered by surface mining, a dredge is used to develop placer deposits. Floatation and other gravity techniques are used for concentration of heavy minerals. This step is done on a floating unit, the dredge digs forward and tailings are stacked behind it. The mining and classification leads to a very wet material which has to be dried for application as bed material in a fluidized bed.

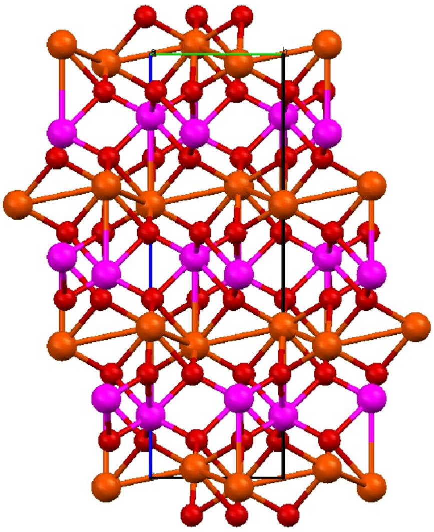

Figure 2.1.: packing structure of ilmenite. red: oxygen, brown: iron, violet: titanium

Since ilmenite is an important raw material for titanium production and also for the production of $TiO_2$ pigments, the reduction and also the oxidation have been investigated in the past. Most of the works have their focus on the reduction of ilmenite, to separate the titanium containing part from the iron. Some researchers found out, that preoxidation already occurs during ball-milling and that preoxidation has a positive effect on the following reduction. According to Nell [15] the following changes in phase chemistry occur during oxidation of ilmenite. The initial step is the formation of $Fe_2O_3 - FeTiO_3$ solid solutions and rutile. Moving on oxidizing the material leads to a content of $Fe_2O_3$ which cannot be accommodated in the solid solution and pseudobrookite ($Fe_2TiO_5$) is then formed. Further oxidation leads to the elimination of $Fe_2O_3$, the stable phases are rutile and $Fe_2TiO_5 - FeTi_2O_5$ solid solutions. Figure 2.2 gives an overview of the $FeO - Fe_2O_3 - TiO_2$ system.

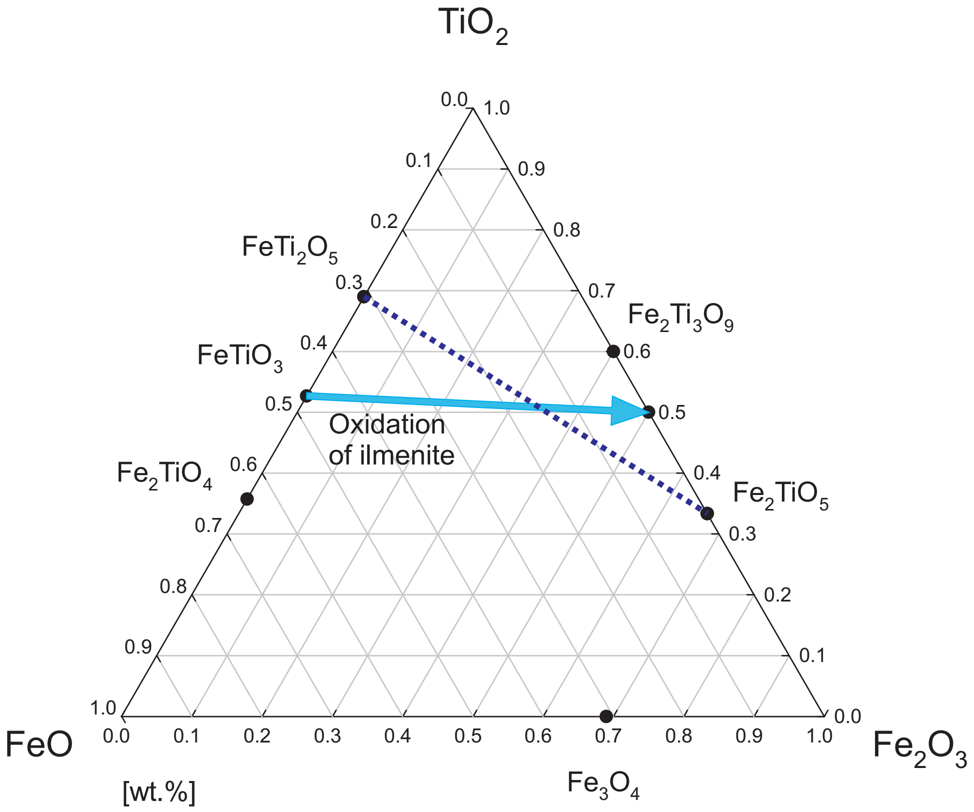

Figure 2.2.: Ternary plot of the $FeO - Fe_2O_3 - TiO_2$ system

According to Nell [15] an enrichment of iron in the hull of the particles occur during oxidation at low temperatures (below 800 °C). The iron-rich layer is the product of a different oxidation mechanism, cations vacancies are introduced in the ilmenite structure. Nell gives the following qualitative approach to explain this phenomena. $O^{2-}$ anions are added to the ilmenite lattice and the electrons needed to form these anions are generated in the oxidation of $Fe^{2+}$ to $Fe^{3+}$.

$$Fe^{2+} \leftrightarrow zFe^{3+} + (1-z)Fe^{2+} + ze^{-} \tag{2.1}$$

$$ze^{-} + {}^{z}\!/_{2}\, O_2 \leftrightarrow {}^{z}\!/_{2}\, O^{2-} \tag{2.2}$$

Equations 2.1 2.2 show the oxidation of $Fe^{2+}$ and the formation of oxygen anions. The content of cations in the lattice is stable and to keep up a cation to anion ratio of 2 to 3, the formation of $(^2/_3)/^z/_2)$ cation vacancies for $^z/_2$ is required. The overall oxidation reaction can be written as:

$$Fe^{2+} + {}^{z}/_{2}\,O \leftrightarrow zFe^{3+} + (1-z)Fe^{2+} + {}^{z}/_{3}\,cation\,vacancy \tag{2.3}$$

The addition of oxygen takes place on the surface, but the electrons needed for the generation of $O^{2-}$ come from within the grain. Oxygen anion diffusion into the grain is slower than the diffusion of cations and this causes a flux of electrons to the surface of the grain. To keep up charge balance the electron flux is compensated by the migration of iron cations to the surface, leading to an accumulation of iron cations on the surface of the grain. At high temperatures cation migration does not take place. This could be explained with the formation of rutile, boundaries between the rutile and the ilmenite grains allow quick diffusion of oxygen. Thermal treatment of ilmenite in an oxidative atmosphere at temperatures of 800 °C or even higher can therefore help avoiding the formation of an iron hull over the particles which can cause agglomerations during CLC operation.

### 2.1.2. Air-reactor reactions using ilmenite

Using ilmenite as oxygen carrier, there are some stages of oxidation available, depending on the temperature and the degree of oxidation of the base material. Chen [17] [18] found that there is one step of oxidation in the temperature range from 600°C to 1000°C. This is important for the first treatment of fresh bed material (compare 3.1.2) to produce fully oxidized particles before starting chemical looping combustion. The product of this first step of oxidation is pseudorutile($Fe_2Ti_3O_9$) which is generated according to the following reaction. The degree of oxidation of the iron part changes from +2 to +3.

$$4FeTiO_3 + O_2 \rightarrow Fe_2Ti_3O_9 + TiO_2 + Fe_2O_3 \tag{2.4}$$

Not only temperature is the driving force for this reaction, according to Grey [19] this reaction also takes place during alteration and weathering of natural ilmenite. According to this, it is possible that a fresh batch of bed material has a small share of pseudorutile. Also this fact shows the requirement of thermal treatment before the first use, to ensure a well defined state of oxidation in the bed.

With increasing temperature pseudorutile becomes unstable. It reacts under oxidising conditions to pseudobrookite ($Fe_2TiO_5$). This configuration is the end-product of oxidation under the conditions in the air-reactor.

$$\begin{aligned} Fe_2Ti_3O_9 &\rightarrow Fe_2TiO_5 + 2TiO_2 \\ Fe_2O_3 + TiO_2 &\rightarrow Fe_2TiO_5 \end{aligned} \tag{2.5}$$

At operational temperature, which lies between 900 °C and 1000 °C, the intermediate step of pseudoruile formation is not available. Ilmenite reacts to pseudobrookite directly. This goes along with the work of Sun [20] who found pseudorutile as oxidation product at 1073K but only pseudobrookite at 1273K. Using ilmenite as bed material, the air-reactor reaction can be written as shown below.

$$2FeTiO_3 + {}^1\!/_2 O_2 \rightarrow Fe_2TiO_5 + TiO_2 \tag{2.6}$$

### 2.1.3. Fuel-reactor reactions using ilmenite

The fuel-reactor reactions could be divided in the oxidation of the fuel and the reduction of the metal oxide, in this case the oxidised form of ilmenite, which is $Fe_2TiO_5 + TiO_2$ (compare 2.1.2).

The fuel oxidation is not a typical combustion of gaseous fuels, because it is not a homogeneous gas/gas reaction but a heterogeneous gas/solid reaction. In contrast to a classical combustion, atomic oxygen is available on the solids surface. Methane has to be activated thermally to produce a $\bullet CH_3$ radical like in normal combustion. This electron transfer sets the oxygen free and the particle is reduced. The possible following reactions show similarities to the proposed reaction paths of methane combustion of the GRI (Gas Research Institute) or the Leeds methane oxidation mechanism, with the limitation of possible reactions with nitrogen or reactions with an excess of oxygen. The main reaction path of methane should follow the following four steps.

$$CH_4 \rightarrow \bullet CH_3 \rightarrow CH_2O \rightarrow CO \rightarrow CO_2 \tag{2.7}$$

According to Leion [21] the reduction starts from prseudobrookite, the oxidised form of ilmenite, $Fe_2TiO_5 + TiO_2$ via the intermediate $Fe_2O_3 \cdot 2TiO_2$ to end up with ilmenite. So the overall solids reaction in the fuel-reactor when using methane as fuel is:

$$4Fe_2TiO_5 + 4TiO_2 + CH_4 \rightarrow 8FeTiO_3 + CO_2 + 2H_2O \tag{2.8}$$

Zhang [22] investigated the reduction of ilmenite with a mixture of methane ($5\,vol.\ \%$), hydrogen ($75\,vol.\ \%$)and argon ($20\,vol.\ \%$). He found out, that preoxidation of ilmenite causes higher reduction temperatures of ilmenite. The formation of metallic iron, while reducing pure, not preoxidised, ilmenite is higher than using preoxidised one. The end product of oxidation is pseudobrookite and rutile when oxidising above 800°C. At temperatures below 800°C only pseudorutile ($Fe_2Ti_3O_9$) is formed. Possible side reactions, which should be avoided, are: the reduction to $Fe\ ^0$ and the reduction of the rutile, which is also possible, according to Zhang [23].

Using syngas Reaction 2.8 changes to:

$$2Fe_2TiO_5 + 2TiO_2 + CO + H_2 \rightarrow 4FeTiO_3 + CO_2 + H_2O \tag{2.9}$$

When using syngas as fuel, two reductive species are present in the fuel-reactor. For the reduction of ilmenite with hydrogen Sun [24] found out that pre-oxidation enhances the following reduction. The reduction itself has two stages. One from $Fe\ ^{3+}$ to $Fe\ ^{2+}$ and a second one from $Fe\ ^{2+}$ to $Fe\ ^0$. The first step is the desired reaction for the fuel-reactor, whereas the second one should be avoided. Reducing to metallic iron causes sticky particles, which leads to defluidization and sintering of the bed material. According to Sun [24] the first step of reduction is:

$$Fe_2O_3 + H_2 \rightarrow 2FeO + H_2O \tag{2.10}$$

The second step, which should be avoided is:

$$FeTiO_3 + H_2 \rightarrow Fe + TiO_2 + H_2O \tag{2.11}$$

According to Sun et al. [25] it is possible to reduce ilmenite with pure hydrogen at temperatures below the operational temperatures in the system. Kucakkaragoz [26] investigated solid state carbothermic reduction of ilmenite. As a consequence of these facts, too long residence times of the solids in the fuel-reactor, in a highly reductive atmosphere, should be avoided. Also defluidization in the upper loop seal could cause problems due to the presence of hydrogen or also carbon on the fuel-reactor side of the siphon, reduction of the bed material could appear and cause agglomeration of the bed material.

A reaction, that would take place in the gas phase of the fuel-reactor, is the water-gas-shift reaction, which has an effect on the carbon monoxide and hydrogen content. The reaction is exothermic, so at high temperatures the equilibrium is on the side of $CO$ and $H_2O$.

$$CO + H_2O \leftrightharpoons CO_2 + H_2 \tag{2.12}$$

The second gas-reaction that will take place in the fuel-reactor is the steam-reforming reaction. As a consequence of the steam concentration in the fuel-reactor, the high temperatures and the absence of free oxygen (no gaseous $O_2$) the presence of this reaction is very likely.

$$CH_4 + H_2O \leftrightharpoons CO + 3H_2 \tag{2.13}$$

## 2.2. Bed material analytics

### 2.2.1. X-ray diffraction

X-ray diffraction (XRD) is a very common method to determine cristalline structures. The phenomenon of x-ray diffraction was first postulated by Max von Laue in 1912. Crystals act as a threedimensional lattice for x-rays, so diffraction is possible. The diffracted beams interfere with each other. Depending on the space between two lattice planes and the incident angle optical retardation occurs and causes constructive and destructive interference. This phenomenon is described by Bragg's law (Equation 2.14) with $d$ as the vertical distance between the lattice planes, $\Theta$ as the diffraction angle, $n$ as the diffraction order and $\lambda$ as the wavelength of the used x-rays.

$$2d \cdot sin\Theta = n \cdot \lambda \tag{2.14}$$

The stucture of a crystal is described by its elementary cell. This cell is defined by six cell parameters, $a, b, c$ and $\alpha, \beta, \gamma$. The parameters $a, b, c$ are the lenghts beteween two lattice planes with the same orientation like one side of the elementary cell, these lattice planes are equal. The parameters $\alpha, \beta, \gamma$ are the angles between the vectors building the structure by translational motion of the elementary cell. These six parameters build a coordinate plane with the basis vectors $\overrightarrow{a}$, $\overrightarrow{b}$ and $\overrightarrow{c}$.
Planes and orientations in the crystal are described by the miller indices $h, k, l$. These indices characterize the plane, which goes through the points $\frac{1}{h}\overrightarrow{a}$, $\frac{1}{k}\overrightarrow{b}$ and $\frac{1}{l}\overrightarrow{c}$. Each reflex in the powder pattern corresponds to a lattice plane described by its miller indices. The whole XRD pattern is characteristic for each substance. By measuring a mixture of substances the pattern is the summation of the pure phase patterns of each substance. A method to get quantitative information from the pattern is the Rietveld method [27]. This method works with the whole pattern. It is necessary to identify all phases present to get the structural data. The computer calculates a pattern from the data and models it until the calculated pattern fits the measured. The refinement fits itself to the data iteratively so no pure phase standards are required and overlapped lines and patterns can be used successfully. The Rietveld method works with two groups of parameters, the first group includes parameters for the position, the halfwidths and possible asymmetry in addition to the property of the powder sample. The second group of parameters stands for the structural properties.

| | |
|---|---|
| U,V,W | halfwidth parameters |
| Z | counter zero point |
| A, B, C, D, E, F | cell parameters according to<br>$\frac{1}{d^2} = Ah^2 + Bk^2 + Cl^2 + Dkl + Ehl + Fhk$ |
| P | asymmetry parameter |
| G | preferred orientation parameter |

Table 2.1.: first group of rietveld parameters

It is possible to calculate a profile with these parameters so a function M, describing the difference between the measured pattern and the calculated, exists which has to be minimized with respect to the parameters.

$$M = \sum_i W_i \{y_{i(obs)} - \frac{1}{c} y_{i(calc)}\}^2 \tag{2.15}$$

A least-squares refinement, using a computer, is carried out. To start the refinement approximate values for all parameters are required. The parameters are

| | |
|---|---|
| $c$ | overall scale factor $y(calc) = c \cdot y(obs)$ |
| $Q$ | overall isotropic temperature parameter |
| $X_i, Y_i, Z_i$ | fractional coordinates of the ith atom in the asymmetric unit |
| $B_i$ | atomic isiotropic temperature parameter |
| $n_i$ | occupation number |
| $\overrightarrow{K}_{x,i}, \overrightarrow{K}_{y,i}, \overrightarrow{K}_{z,i}$ | components of the magnetic vector of the ith atom in the asymmetric unit |

Table 2.2.: second group of rietveld parameters

refined in the calculation cycles until a certain convergence criterion has been reached.

### 2.2.2. Thermo gravimetric analysis

Thermo-gravimetric analysis (TGA) is a part of thermal analysis. The change of mass as a function of temperature and time is measured. The sample is usually placed in a platinum- or alumina-oxide- crucible which is connected with a micro-scale. The whole setting is placed in an oven, temperature regulation is done depending on the temperature of the crucible. During analysis the oven is typically flooded with nitrogen as inert medium to avoid oxidation. In special cases, reductive and oxidative atmospheres can be provided in the measuring cell. The effects which will cause a change of sample weight are:

- Physical processes (e.g.: evaporation, sublimation)
- Decomposition (e.g.: production of volatiles from the sample)
- Decrease of mass from chemical reaction (e.g.: due to reduction of the sample)
- Increase of mass from chemical reaction (e.g.: due to oxidation of the sample)

Since temperature, weight and time are measured TGA is a common way to determine reaction kinetics. If only one reaction takes place and the sample is stable in the temperature range, the change in mass corresponds to the progress of the reaction.

## 2.3. Fluidized beds

### 2.3.1. Particle properties

To make the classification of the fludization properties of different powders easier, Geldart [28] introduced four categories of solids powders. These four groups are shown in Table 2.3 with their main properties.

| | |
|---|---|
| Group C: | These particles are very fine ($d_p \leq 20\mu m$) and cohesive. Also very irregular formed particles fit into this group. Fluidizing these materials is very difficult, they tend to build channels and plugs when fluidized. An example for this category is flour. |
| Group A: | Powders in this group show quite fine particle diameters ($d_p$ from $30-100\mu m$), cohesion exists but is much lower than in group C. Particles in this group show good fluidization properties, between $U_{mf}$ and $U_{mb}$ the fluidized bed expands homogeneously. Many cracking catalysts show group A behaviour. |
| Group B: | Particles in this group are of intermediate size ($d_p$ from $100-800\mu m$). They show no cohesive forces between the particles. A homogeneous phase does not exist, bubbling starts as soon as $U_{mf}$ is reached. Due to the heavy bubbling solids mixing in the bed is excellent. Sand fits in this group very well. |
| Group D: | Coarse particles ($d_p \geq 1mm$) and particles with high densities fit in this group. The regime is only spouting and solids mixing is rather poor. Corn and coffee beans can be found in this group. |

Table 2.3.: Powder classification according to Geldart [28]

The boundaries between the different groups were proposed by Geldart [28] in form of a dimensional plot of $\Delta\rho$ vs. $d_p$. Grace [29] summarized the works of different researchers on the identification of the boundaries between the four groups. For the C-A boundary, Grace [29] proposes the following equation:

$$(d_p^*)_{CA} \approx 0.68 \text{ to } 1.1 \quad \text{or} \quad Ar_{CA} \approx 0.31 \text{ to } 1.3 \tag{2.16}$$

The difference between Group A and Group B is the fact, that for Group A a range between $U_{mf}$ and $U_{mb}$ exists, whereas in group B $U_{mf}$ is equal to $U_{mb}$. Grace [29] recommends the following equation to estimate the AB boundary region.

$$(d_p^*)_{AB} = 101({}^{\Delta\rho}/_{\rho_g})^{-0.425} \quad \text{or} \quad Ar_{AB} = 1.03 \times 10^6({}^{\Delta\rho}/_{\rho_g})^{-1.275} \tag{2.17}$$

To define the B-D boundary, Grace [29] uses the following conditions.

$$(d_p^*)_{BD} = 53 \quad \text{or} \quad Ar_{BD} = 1.45 \times 10^5 \tag{2.18}$$

In Figure 2.3 these suggested boundaries are shown. Also the typical working areas of fluidized industrial reactors can be found. As shown, the typical bed material for fluidized and also circulating beds is a Geldart type A or type B particle.

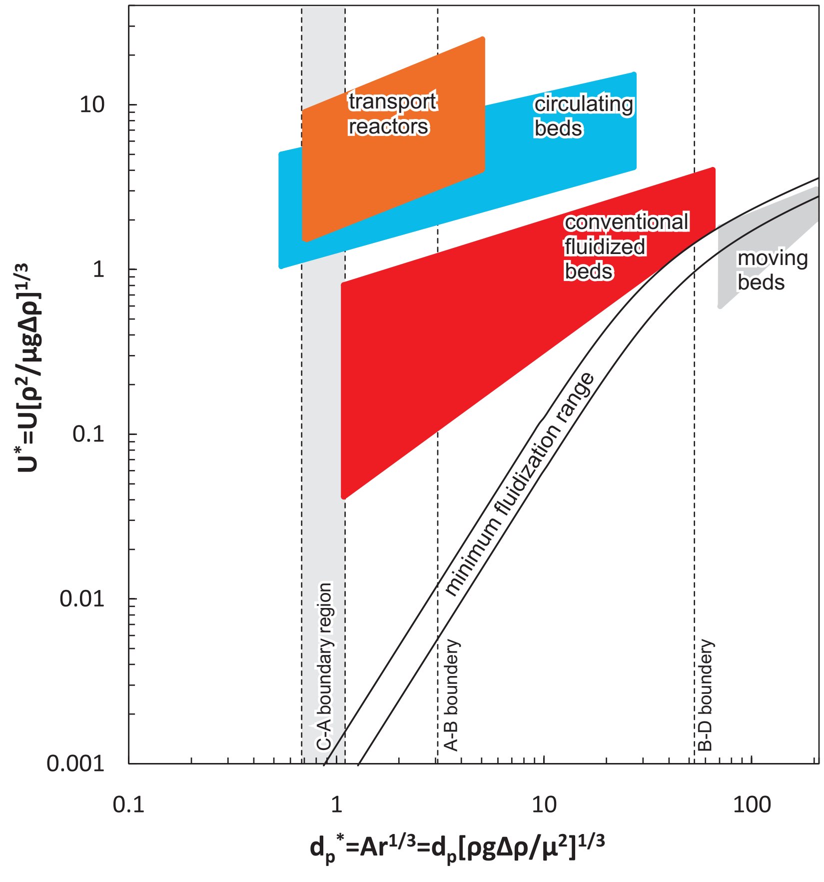

Figure 2.3.: diagram according to Grace [29] dimensionless superficial gas velocity *vs.* dimensionless particle diameter

### 2.3.2. Bubbling fluidized beds

Apart from the particle size and the particle spericity, the superficial gas velocity ($U$) in the reactor is an important factor to describe a fluidized bed operation.

$$U = \frac{\dot{Q}}{A} \tag{2.19}$$

The fluidizing gas experiences a resistance when it moves through the bed. This leads to a pressure drop ($\Delta p$) which is proportional to the height of the bed. Increasing gas velocity has no effect on the pressure drop in the bed, it is almost constant in the range between minimum fluidization velocity ($U_{mf}$) and terminal velocity ($U_t$). At the point, when fluidization starts, the gravitational force of the bed is equal to the pressure drop of the fluidizing medium. This relation is shown in Equation 2.20. Using this condition, the pressure drop can be calculated as shown in Equation 2.21.

$$\Delta p \cdot A = A \cdot (1 - \epsilon_{mf}) \cdot (\rho_p - \rho_g) \cdot g \cdot H_{mf} \tag{2.20}$$

$$\Delta P = (1 - \epsilon) \cdot (\rho_p - \rho_g) \cdot g \cdot H \tag{2.21}$$

The porosity of the fluidized bed can be written as a function of the density of the fluidized bed and particle density as shown in Equation 2.22.

$$\epsilon = 1 - \frac{\rho_b}{\rho_p} \tag{2.22}$$

The point of minimum fluidization can be described as the point, where the pressure drop of the fluidized bed is equal to the pressure drop of the fixed bed. The pressure drop of a fixed bed can be calculated using the Ergun equation (Equation 2.23).

$$\frac{\Delta p}{H} = 150 \cdot \frac{(1-\epsilon)^2}{\epsilon^3} \cdot \frac{\mu_g \cdot U}{(\varphi_p \cdot d_p)^2} + 1.75 \cdot \frac{1-\epsilon}{\epsilon^3} \cdot \frac{\rho_g \cdot U^2}{\varphi_p \cdot d_p} \tag{2.23}$$

Using Equations 2.21 and 2.23 and the condition that the pressure drop of the fixed bed is equal to the one of the fluidized bed at the loosening point, leads to the following equation.

$$
\begin{aligned}
(1-\epsilon_{mf}) \cdot (\rho_p - \rho_g) \cdot g = 150 \cdot \frac{(1-\epsilon_{mf})^2}{\epsilon_{mf}^3} \cdot \frac{\mu_g \cdot U_{mf}}{(\varphi_p \cdot d_p)^2} + \\
+1.75 \cdot \frac{1-\epsilon_{mf}}{\epsilon_{mf}^3} \cdot \frac{\rho_g \cdot U_{mf}^2}{\varphi_p \cdot d_p}
\end{aligned}
\tag{2.24}
$$

The dimensionless form of Equation 2.24 can be written as:

$$
\begin{aligned}
\frac{(d_p \cdot \varphi_p)^3 \cdot \rho_g \cdot (\rho_p - \rho_g) \cdot g}{\mu_g^2} = 150 \cdot \frac{(1-\epsilon_{mf})}{\epsilon_{mf}^3} \cdot \frac{\rho_g \cdot d_p \cdot \varphi_p \cdot U_{mf}}{\mu_g} + \\
+ \frac{1.75}{\epsilon_{mf}^3} \cdot \frac{\rho_g^2 \cdot (\varphi_p \cdot d_p)^2 \cdot U_{mf}^2}{\mu_g^2}
\end{aligned}
\tag{2.25}
$$

Using the following definitions for the Ar-Number (Equation 2.26), the Re-Number (Equation 2.27) and the correlation between the particle diameter and the sphericity Equation 2.25 can be written as:

$$
Ar = \frac{\rho_g \cdot d_p^3 \cdot (\rho_p - \rho_g) \cdot g}{\mu^2} \tag{2.26}
$$

$$
Re = \frac{\rho_g \cdot U \cdot d_p}{\mu} \tag{2.27}
$$

$$
d_{sv} = \varphi_p \cdot d_p \tag{2.28}
$$

$$
Ar = C_1' \cdot Re_{mf} + C_2' \cdot Re_{mf}^2 \tag{2.29}
$$

with:

$$
C_1' = 150 \cdot \frac{(1-\epsilon_{mf})}{\epsilon_{mf}^3 \cdot \varphi^2{}_p} \quad , \quad C_2' = \frac{1.75}{\epsilon_{mf}^3 \cdot \varphi_p} \tag{2.30}
$$

Solving this quadratic Equation 2.29 leads to the following form to calculate $Re_{mf}$:

$$
Re_{mf} = (\sqrt{C_1'^2 + 4C_2' Ar} - C_1') \cdot \frac{1}{2C_2'} \tag{2.31}
$$

Since the density of the bubbling bed is not accessible and the results are depending on the particle spericity, which is also unknown, empirical correlations are used to calculate $Re_{mf}$. These correlations base on the measurement of the pressure drop of the bed. Literature shows many values for $C'_1$ and $C'_2$. Bi and Grace [30] use the correlation shown in Equation 2.32 which also leads to realistic values of $\varphi_p$ and $\epsilon_m f$, namely 0.898 for the spericity and 0.43 for the density of the bed.

$$Re_{mf} = \sqrt{27.2^{\,2} + 0.0408\,Ar} - 27.2 \tag{2.32}$$

To determine the upper end of bubbling fluidized beds, the terminal velocity ($U_t$) is introduced. It can be calculated using the force balance of all forces affecting a free falling particle. These forces are: gravitational force, friction, uplift and acceleration. Using a spherical particle, the force balance can be written like Equation 2.33.

$$\frac{\pi}{6} \cdot d_s^3(\rho_p - \rho_g) \cdot g - C_W \cdot A_p \cdot \frac{\rho_g \cdot U_t^2}{2} = \frac{\pi}{6} \cdot d_s^3 \cdot \rho_p \cdot \frac{dU_t}{dt} \tag{2.33}$$

In the case of a floating particle, acceleration reaches zero and the floating velocity can be written as follows:

$$U_t = \sqrt{\frac{4}{3} \cdot \frac{\rho_p - \rho_g}{\rho_g} \cdot \frac{d_s \cdot g}{C_W}} \tag{2.34}$$

The drag coefficient is contingent on the conditions of the fluid flow. These conditions are described by the Reynolds Number which has to be calculated as shown in Equation 2.27. Three flow ranges can be described, a laminar flow area, a turbulent flow area and a transition section. For a spherical particle the floating velocity in the laminar area ($Re < 0.2$) can be described as shown in Equation 2.35. The turbulent area ($Re > 1000$) is described in Equation 2.36. The flow range in the transition section ($0.2 < Re < 1000$) has to be described through iteration or numerical solving. The drag coefficient in the transition section is shown in Equation 2.37

$$C_{W,laminar} = \frac{24}{Re} \qquad \rightarrow U_{t,laminar} = \frac{(\rho_p - \rho_g \cdot g \cdot d_s^2}{18 \cdot \mu} \tag{2.35}$$

$$C_{W,turbulent} = 0.43 \qquad \rightarrow U_{t,turbulent} = \sqrt{\frac{4}{3} \cdot \frac{\rho_p - \rho_g}{\rho_g} \cdot \frac{g \cdot d_s}{0.43}} \tag{2.36}$$

$$C_{W,transition} = \frac{24}{Re} + \frac{4}{\sqrt{Re}} + 0.4 \tag{2.37}$$

### 2.3.3. Circulating fluidized beds

Bi and Grace [30] describe the different stages of fluidization. Starting with a fixed bed the states of bubbling fluidization, slugging fluidization, turbulent fluidization and pneumatic transport can be achieved by increasing the gas velocity in the riser. Figure 2.4 shows these different states of fluidization with increasing gas velocity from left to right.

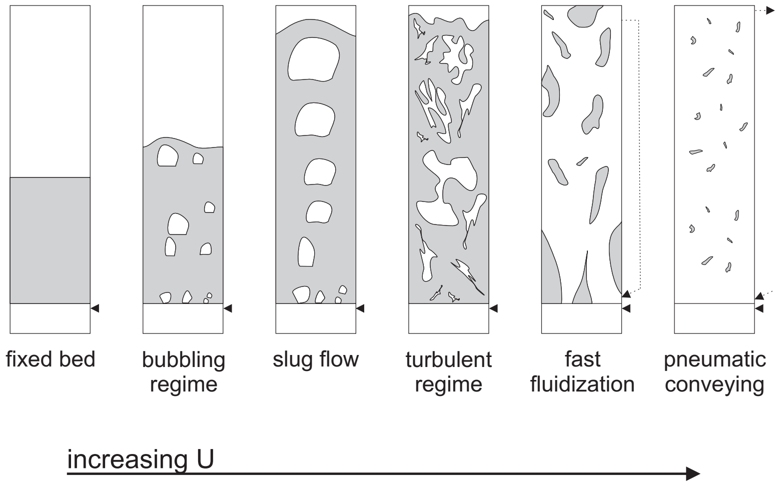

Figure 2.4.: flow patterns of fluidized beds as a function of fluidization velocity [31]

The minimum fluidization velocity, $U_{mf}$, which is necessary to move on from a fixed bed to a fluidized bed can be determined experimentally. Equation 2.31 gives a basic approach to determine $Re_{mf}$ and Equation 2.38 gives realistic results for $U_{mf}$ and can also be written as follows:

$$U_{mf} = \frac{\mu_g}{\rho_g \cdot d_p} \cdot (\sqrt{27.2^{\,2} + 0.0408\,Ar} - 27.2) \tag{2.38}$$

The start of bubble formation in the bed is set by the minimum bubbling velocity, $U_{mb}$. This velocity depends strongly on particle properties. For Group A particles from the Geldart classification (compare section 2.3.1) $U_{mb}$ is higher than $U_{mf}$, but for Group B and Group D particles these two velocities are equal. For fine Group A particles $U_{mb}$ can be estimated by the Geldart and Abrahamsen [32] dimensional correlation.

$$U_{mb} = 33\,d_p\,\left(\frac{\rho_g}{\mu}\right)^{0.1} \tag{2.39}$$

With increasing gas velocities the bubbles become larger and larger until they have a comparable diameter with the reactor. This is the point where slugging occurs as explained in section 2.3.4 below. According to Steward and Davidson (1967) the minimum slugging velocity, $U_{ms}$, can be calculated with the following equation.

$$U_{ms} = U_{mf} + 0.007\,\sqrt{g\,D} \tag{2.40}$$

According to Bi and Grace [30] slugging does not occur in shallow beds, in columns of very large diameter and in beds of fine particles, because the bubbles have no chance to grow until they reach the required size for slugging.
To describe the operating point where the bubbling regime changes to a turbulent regime the change of the pressure drop can be used. This gas velocity, $U_c$, can be predicted [30] by

$$Re_c = 1.24\,Ar^{\,0.45} \qquad \left(2 < Ar < 1 \times 10^{\,8}\right). \tag{2.41}$$

To determine the change from turbulent to fast fluidization Bi and Grace [30] use the solids entrainment velocity, $U_{se}$. The following correlation has been developed for estimating $U_{se}$ [30]

$$Re_{se} = 1.53\, Ar^{\,0.50} \qquad \left(2 < Ar < 4 \times 10^{\,6}\right) \tag{2.42}$$

It is useful to draw a flow regime diagram to get an impression of the fluidization regime of a certain application. Bi and Grace [30] recommend the use of a dimensionless flow regime map with the dimensionless velocity $U^*$ versus the dimensionless particle diameter $d_p^*$ as axes. Equation 2.43 shows the definition of these two parameters.

$$U^* = \frac{Re}{Ar^{1/3}} \qquad d_p^* = Ar^{1/3} \tag{2.43}$$

When using the equations for the transition velocities (Equations 2.34, 2.32, 2.41 and 2.42) and the dimensionless axes (Equation 2.43) it it possible to draw a flow regime map as shown in Figure 2.5. In this diagram, all relevant fluidization regimes are present. In the area between $U_{mf}^*$ and $U_c^*$ bubbling fluidized beds can be found. The section between $U_c^*$ and $U_{se}^*$ stands for regimes of turbulent fluidization. At higher $d_p^*$ and below $U_{mf}^*$ moving beds are located.

### 2.3.4. Bubbles in fluidized beds

Bubbles in fluidized beds behave like bubbles in liquids of low viscosity. To describe this phenomenon the following assumption is taken. The bubbles are free of solids and particles move aside as bubbles rise. According to Kunii and Levenspiel [33] the rise velocity of a single bubble in a fluidized bed can be calculated as shown in equation 2.44.

$$U_{br} = 0.711 \cdot (gd_b)^{\frac{1}{2}} \;, \qquad \frac{d_b}{dt} < 0.125 \tag{2.44}$$

Bigger bubbles with $\frac{d_b}{dt} > 0.125$ will interfere with the walls and bubbles with a diameter bigger than 60% of the reactor diameter will cause slugging. In both cases equation 2.44 can not be used.
Kunii and Levenspiel [33] assume, that all the gas in excess of $U_{mf}$ forms bubbles of equal size. The density of the fluidized bed without the bubbles is constant and

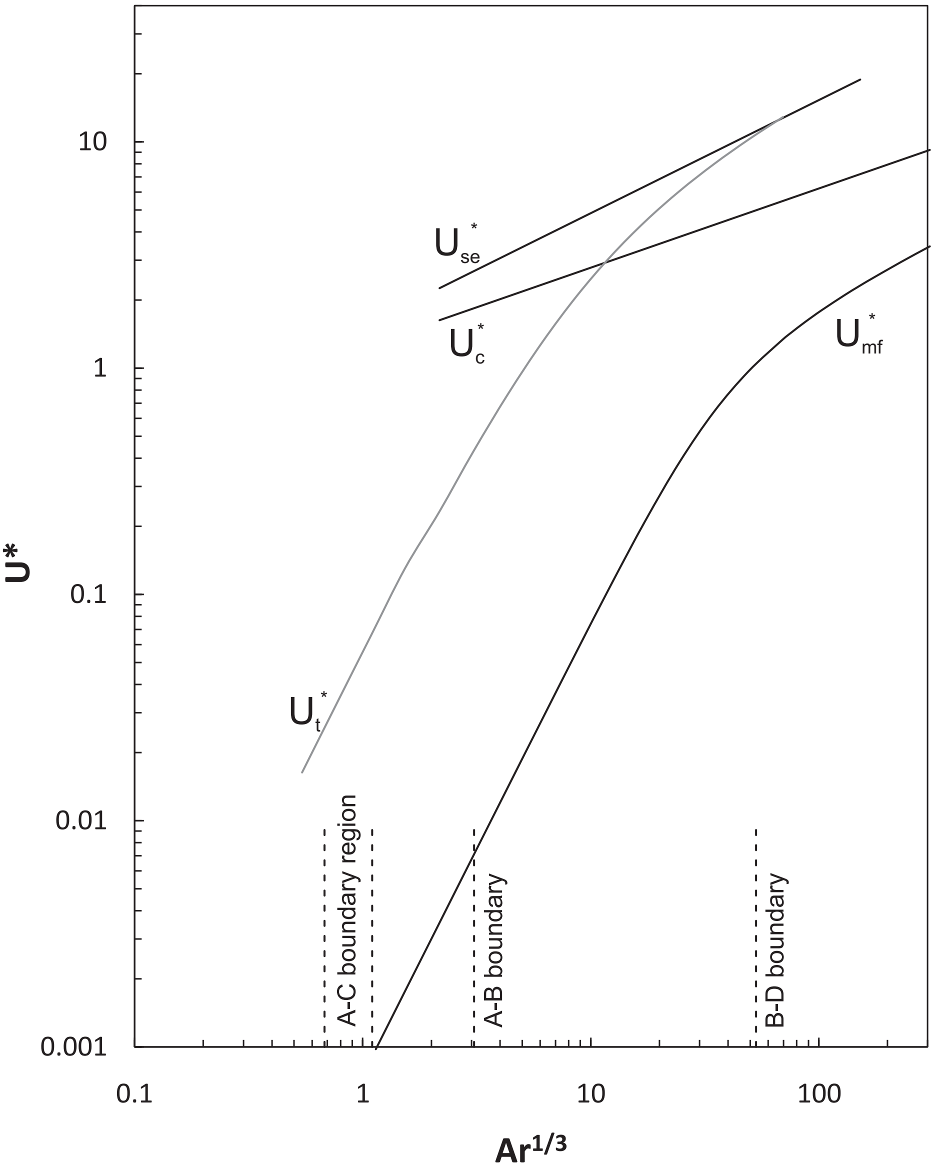

Figure 2.5.: Flow regime map according to Grace [31]

equal to minimum fluidization. The volumetric flow of gas from a single orifice $\dot{V}_{or}$, which forms the bubble, can be calculated with the following expression.

$$U - U_{mf} = \dot{V}_{or} \cdot N_{or} \tag{2.45}$$

The number of orifices can be calculated as shown in the following equations

$$\begin{aligned} N_{or} &= \frac{1}{l_{or}^2} && \text{for a square array of holes} \\ N_{or} &= \frac{2}{\sqrt{3} \cdot l_{or}^2} && \text{for an equilateral triangle array of holes} \end{aligned} \tag{2.46}$$

At low gas flow rates the initial bubbles are smaller than the distance between two adjacent orifices. They do not touch each other. According to [33] the bubble size can be written as

$$d_{b0} = 1.30 \cdot \frac{\dot{V}_{or}^{0.4}}{g^{0.2}} \tag{2.47}$$

Using equations 2.45 and 2.47 the initial bubble size for low gas flow rates can be calculated as shown in equation 2.48.

$$d_{b0} = \frac{1.30}{g^{0.2}} \cdot \left( \frac{U - U_{mf}}{N_{or}} \right)^{0.4} \quad , \qquad d_{b0} \le l_{or} \tag{2.48}$$

At high gas flow rates the initial bubbles are bigger than the spacing between two orifices. They touch and overlap when formed, so equation 2.48 can not be used. In this case the initial bubble size is equal to the distance between two holes, the bubbles are just touching. Using equation 2.46 this condition is given for a triangle array of touching bubbles as shown in the following equation.

$$d_{b0}^2 = \frac{2}{\sqrt{3} \cdot N'_{or}} \tag{2.49}$$

$N'_{or}$ represents the fictitious orifice spacing that corresponds to the touching bubbles. Using $N'_{or}$ instead of $N_{or}$ in equation 2.48 the initial bubble size at high gas flow rates can be written as shown in equation 2.50.

$$d_{b0} = \frac{2.78}{g} \left( U - U_{mf} \right)^2 \quad , \qquad d_{b0} > l_{or} \tag{2.50}$$

Using a porous plate distributor, which can be assumed as an array of numerous tiny triangular arranged holes, equation 2.50 fits very well to describe the bubble formation above the distributor.
According to [33] bubble size increases with gas velocity and with height above the distributor. Fluidizing tall and narrow beds, bubbles can grow until they form

slugs. Fine particles of good fluidity will rain down at the bed wall and axial slugs will occur. With increasing gas velocity and at rough vessel walls the rising slugs adhere and slide up the wall. The slugs caused be this phenomenon are called wall slugs. Large Geldart D particles cause flat slugs. The bed is separated into slices of emulsion separated by gas. In figure 2.6 the three types of slugging are shown. The rise velocity of a single slug is given in equation 2.51 [33].

$$U_{br} = 0.35 \cdot (g \cdot d_t)^{\frac{1}{2}} \tag{2.51}$$

Since the bubble growth depends on the bubble rise velocity and on the hight above the distributor it is useful to define boundary conditions to avoid slugging. According to Kunii and Levenspiel [33] slugging should not occur below the following bubble rise velocity.

$$U_{b,ms} = U_{mf} + 0.07\,(g \cdot d_t)^{\frac{1}{2}} \tag{2.52}$$

The height in the bed below which no slugs will be formed is

$$z_s = 60 \cdot d_t^{0.175} \tag{2.53}$$

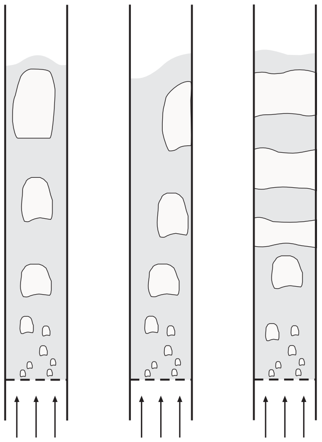

Figure 2.6.: Three types of slugs formed in fluidized beds: left: axial slugs, middle: wall slugs, right: flat slugs [33]

# 3. Practical part

## 3.1. The 120kW test rig

The rig was designed as a dual circulating fluidized bed (DCFB) system (Figure 3.1). This reactor system consists of two reactors, the air-reactor and the fuel-reactor. These two reactors are interconnectet with two loop seals which are moderately fluidized with steam to prevent gasmixing between the reactors. To support solids circulation the lower loop seal has a support fluidization in the connection tubes between reactors and loop seal. Also the support fluidization is run with steam. The fuel-reactor has his own return leg for inner circulation, also with a steam fluidized loop seal. As a consequence of this design it is important to distinguish between the global solids circulation between the air-reactor and the fuel-reactor and the internal solids circulation in the fuel-reactor.

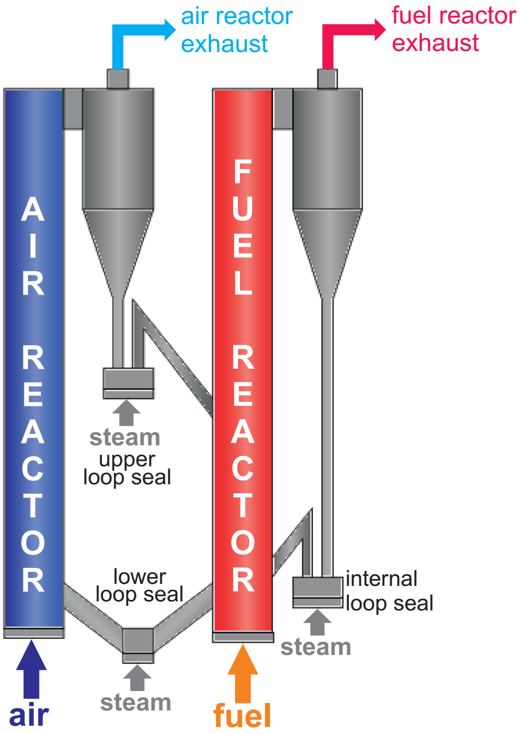

Figure 3.1.: DCFBscheme

The air-reactor is fluidized with air, supplied from a rotary screw compressor. Via the support fluidization in the pipe between loop seal and air-reactor a gaseous fuel can be added. In all cases propane or methane were used for additional heat input in the air-reactor. According to Grace [31] the air-reactor is run in a turbulent fluidization regime. The air-reactor operating area during the test runs was between 85 $Nm^3/h$ and 125 $Nm^3/h$. The operating points are shown in Figure 3.4. To stabilize the temperatures and make higher fuel loads possible, a cooling system is installed on the air-reactor side. Three cooling jackets are mounted round the air-reactor as shown in Figure 3.3. The cooling medium is steam from the steam drum, which is fed from the heat exchangers installed after the cyclones and the fire tube boiler. The superheated steam is cooled down and condensed. The condensate flows into the drain. For start-up and also as additional heat input at low load points an electric air preheater is installed. By using the air preheater two limiting factors occur. The minimum air flow of 60 $Nm^3/h$ to prevent overheating of the device. The second factor is the nozzle velocity in the air-reactor. High velocities lead to milling of the particles and to a decrease of particle size and, as a consequence of this, to a loss of bed material through the cyclones. The maximum nozzle velocity was 50 $m/s$. To gain more degrees of freedom in fluidizing the air-reactor a secondary air-support is installed. The total air is divided via a three way valve in primary air and secondary air. The secondary air is not preheated. With this setup it is possible to increase the total air to the air-reactor without any influence of the global solids circulation. Nozzle velocities are reduced too, by increasing the amount of secondary air.

The fuel-reactor is only fluidized with the gaseous fuel. In this study methane and a model syngas mixture of carbon monoxide and hydrogen in a rate of 1:1 were used. Operating points from 20 $kW$ to 120 $kW$ with methane and from 45 $kW$ to 100 $kW$ with the model syngas, had been investigated. In Figure 3.4 two cases of both fuels are shown for conversion rates from zero to one. During the start-up procedure heat input is needed. To supply this energy a burner with a thermal power of 40 $kW$ is installed in the fuel-reactor as shown in Figure 3.3. The burner is run with methane and has a primary and secondary air support to adjust the flame temperature.

The global solids circulation rate can be controlled with the fluidization rate of the air-reactor. By reducing the rate of solids circulation the residence time of the particles in each reactor is prolonged, whereas only the gas residence time in the air-reactor is affected. The gas solids contact time in the fuel-reactor is only a function of the fuel load and the expansion of the bed. The benefit of the DCFB setup is, that no high temperature valve between the reactors is needed to control global solids circulation.

Both exhaust gas streams are cooled in heat exchangers (compare Figure 3.2) to about 420 °C in the air-reactor stream and about 320 °C in the fuel-reactor stream to enable gas measurement without high temperature equipment. The two streams are mixed in the fire tube boiler. In this unit burnable gases are converted by a methane powered burner, to ensure safe operation without producing explosive gas mixtures in the bag filter or in the chimney. The fire tube boiler is also a heat exchanger, the off gas is cooled down to 170 °C before entering the bag filter. After this last cleaning step the exhaust gas stream enters the chimney.

To make operating the rig easy, a programmable logic controller (PLC) is installed. All measured values (compare 3.3.2, 3.3.3) are sent to the PLC, which is connected to the personal computer running a visualisation of the process. The visualisation is also responsible for data logging. Via the visualisation and the PLC it is possible to control the valves for the air streams to the air reactor, the methane flow to the fuel reactor, the secondary air of the burner in the fire tube boiler and the water feed to the steam drum. A security procedure is also integrated, in case of emergency the methane feed is stopped via a magnetic valve (currentless closed) and the pipe is purged with nitrogen.

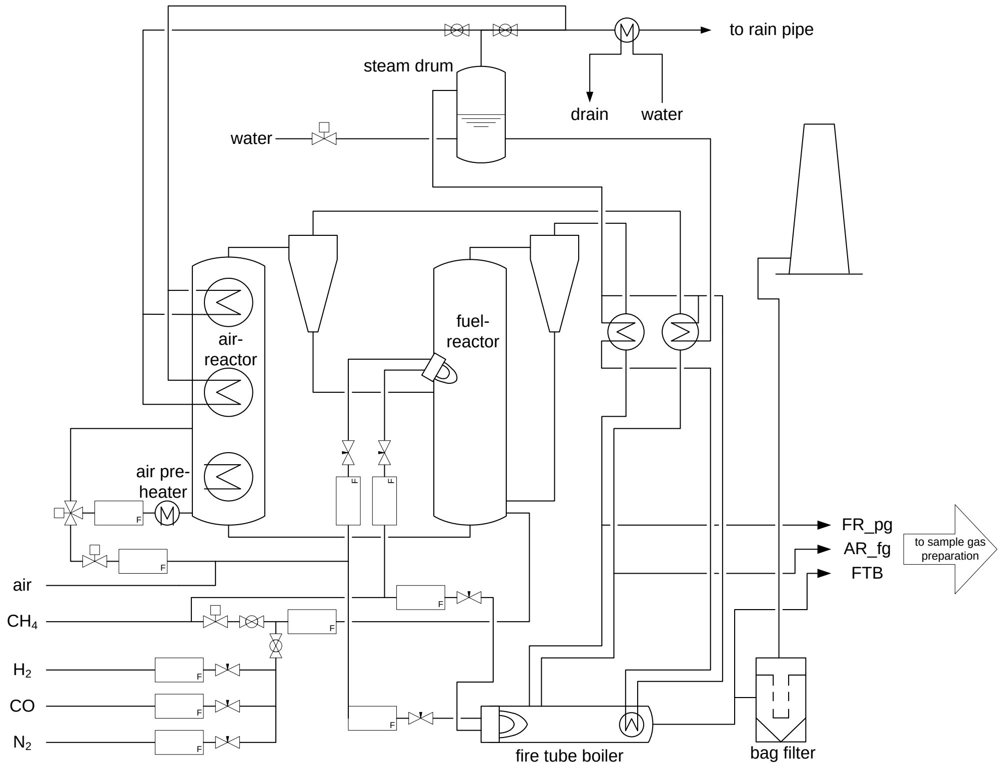

Figure 3.2.: flow chart of the rig (secondary air streams to both burners are not shown here)

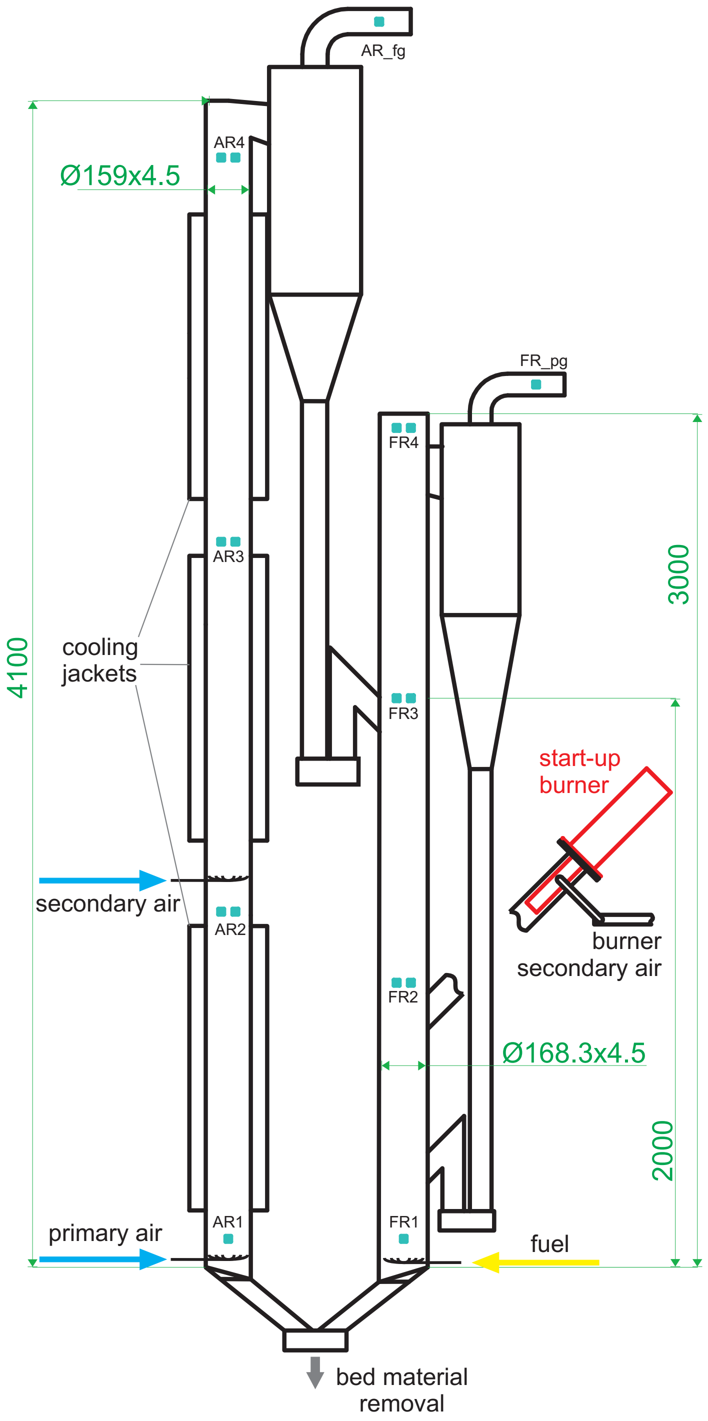

Figure 3.3.: sheer plan of the reactors

### 3.1.1. Operating range

The rig was designed for gaseous fuels and a designed, nickel-based particle. The ilmenite used in the test-runs has not the same dimensions as the nickel-particles [34]. These particles have an average particle diameter of 135 $\mu m$ and a density of 3600 $kg/m^3$. Even though the used ilmenite particles fit in the operative range of the rig as shown in Figure 3.4. They have an average particle diameter of 180 $\mu m$ and their density is 4700 $kg/m^3$. Table 3.1 gives an overview of the bulk geometry and the design data for the rig.

| Parameter | Unit | Value AR | Value FR |
|---|---|---|---|
| Reactor inner diameter | $[m]$ | 0.150 | 0.159 |
| Reactor height | $[m]$ | 4.1 | 3.0 |
| Height of primary gas inlet | $[m]$ | 0.025 | 0.06 |
| Height of secondary gas inlet | $[m]$ | 1.325 | – |
| Inlet gas flow | $[Nm^3/h]$ | 138.0 | 12.0 |
| Outlet gas flow | $[Nm^3/h]$ | 113.9 | 35.9 |
| Temperature in reactor | $[K]$ | 1213 | 1123 |
| Design fluid for calculation | $[-]$ | depleted air | $H_2O/CO_2 = 2/1$ |
| Mean particle size | $[mm]$ | 0.12 | 0.12 |
| Particle apparent density | $[kg/m^3]$ | 3200 | 3200 |
| Particle sphericity | $[-]$ | 0.99 | 0.99 |
| Archimedes number | $[-]$ | 7.55 | 9.13 |
| Superficial velocity | $[m/s]$ | 7.32 | 2.08 |
| Ratio $U/U_{mf}$ | $[-]$ | 1280.4 | 315.4 |
| Ratio $U/U_t$ | $[-]$ | 15.5 | 3.8 |
| Fuel power(natural gas) | $[kW]$ | 120 | 120 |
| Lower heating value of fuel | $[MJ/kg]$ | 48.8 | 48.8 |
| Design air/fuel ratio | $[-]$ | 1.2 | 1.2 |

Table 3.1.: Bulk geometry and design data of the 120$kW$ unit [35]

The air-reactor is designed as a riser, it is a tube with an inner diameter of 15 $cm$. The height of the air-reactor is 4.1 $m$. Turbulent fluidization is needed to offer solids circulation. As a consequence of this the operating range in the air-reactor at 970 °C is between 85 $Nm^3/h$ and 125 $Nm^3/h$ air without any additional fueling in the air-reactor as shown in Figure 3.4. Under these conditions the retention time of the gas in the air-reactor is between 0.76 $s$ at 85 $Nm^3/h$ and 0.51 $s$ at 125 $Nm^3/h$. The gas velocity varies between 5.42 $m/s$ and 7.97 $m/s$.

The fuel-reactor is designed to run in a highly expanded bubbling-bed or also in a turbulent regime. As shown in Figure 3.4 the fluidization pattern is a function of fuel conversion. This is especially the case for methane as fuel, where the gas volume triples by conversion according to Reaction 2.8. Especially with methane as fuel, the flow regime is dependent upon conversion. The inner diameter of the fuel-reactor is taller than the air-reactors, it measures 15.9 $cm$. Due to the lack of space in the technical laboratory the fuel-reactor height is only 3 $m$. According to this design the gas velocities at fuel-reactor exit vary between 0.11 $m/s$ and 2.05 $m/s$ in the methane case. Using the model syngas, gas velocities are between 0.74 $m/s$ and 1.71 $m/s$. In this operational area the average gas residence time in the fuel-reactor lies between 26.32 $s$ and 1.46 $s$ with methane and between 4.06 $s$ and 1.75 $s$ with the carbon monoxide hydrogen mixture. The limiting factor for the fuel-reactor is not the nozzle velocity but the thermal design power. The rig was designed for a maximum thermal load of 120 $kW$ methane. With the model syngas the limiting factor is the gas source. While methane comes from the local gas distribution system, hydrogen, carbon monoxide and nitrogen come from gas cylinders. Higher load points than 100 $kW$ are not convenient due to the high frequency of replacing empty gas cylinders, which limits the duration of stable operating points.

Another limitation in fluidizing the reactors are the cyclones, especially the inlet paths. As a consequence of the design of the cyclones [37] the flow cross-section in the inlet path areas reduces, so the gas velocity increases and the particle stress too. It is not possible to increase global solids circulation arbitrarily, because this would lead to particle abrasion and to a loss of solids as a consequence of separation limitation in the cyclones. Also the separation rate is a function of the inlet velocity into the cyclones, according to the design proposal from Hugi [37] an optimal working area exists. Increasing of gas velocities to values higher than the design limit may lead to bad separation rates.

### 3.1.2. Typical work flow of a test run

The typical work flow is described by means of the collected data during test run No.7 (compare 4.1.1). In this experiment ilmenite was the bed material for start up and the first part of the experiment, a load variation. In the second part 15 $kg$ of olivine were added and the load variation from part one was done again. The fuel was methane and the load range was 20 $kW$ to 120 $kW$ thermal power. Eleven load points were investigated. The whole experiment could be divided into 3 parts, the start up sequence, the measuring of different operating points and the shut down sequence.

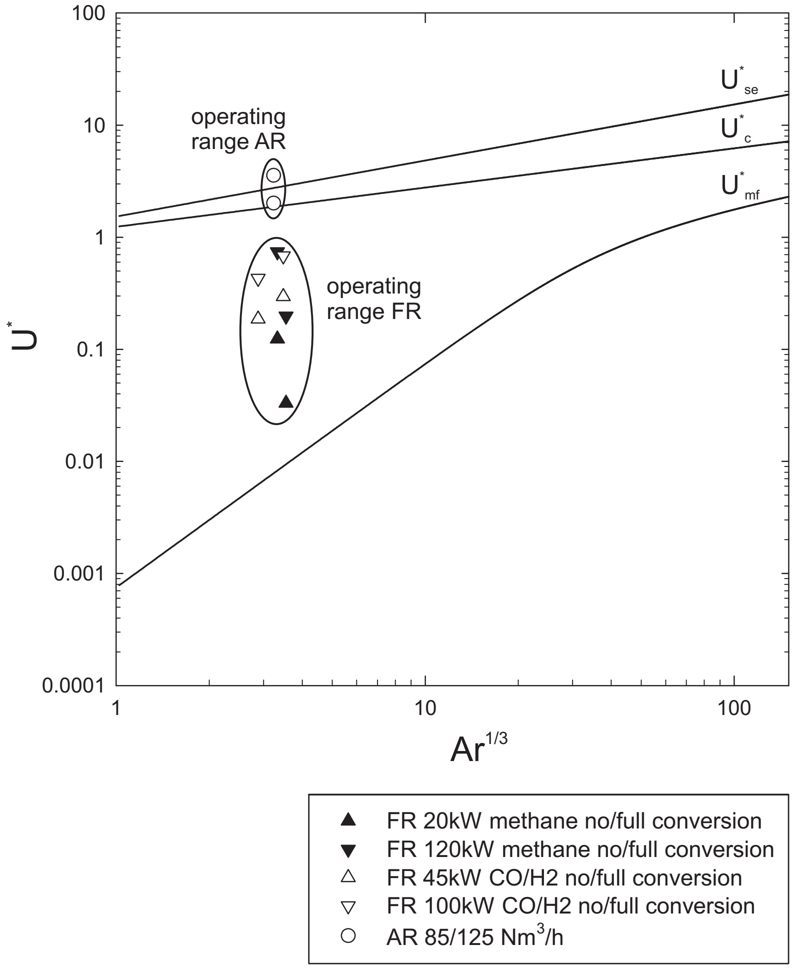

Figure 3.4.: operating range in the flow regime map [36]

### pretreatment of ilmenite

Due to fluidization problems using fresh ilmenite (compare 4.4, 2.1.3) a thermal treatment of the bed material was done. The new batch of bed material was held at a temperature of 800 °C for about six hours in an oxidative atmosphere in both reactors. Afterwards the rig was cooled down and the bed material was ready to be used in the experiments.

### start up

The reactor system was filled with 55 $kg$ of ilmenite. At first the fuel-reactor fluidization was started. The fluidizing medium was air and the amount was about 10 $Nm^3/h$. Afterwards the loop seals were fluidized with air too. At least the air-reactor fluidization was started. The next step was the ignition of the burner in the fire tube boiler. Afterwards the start up burner was ignited and the burner temperature was controlled by increasing or decreasing the secondary air support of the burner. As next step the air preheater was switched on. The temperature set varied as a consequence of the total air flow to the air reactor. With this setup the rig was heated up to 500 °C in the bed. After reaching this temperature the fuel-reactor fluidization was switched to nitrogen and a little flow of hydrogen was added to the fuel-reactor. The conversion was controlled with the online gas analizer (compare section: 3.3.1). Another indication for conversion in the bed are the temperature curves. After stable conversion of hydrogen in the fuel-reactor also the air-reactor got additional heat input with hydrogen. Under these conditions the bed was heated up to 700 °C. After reaching this temperature the additional air-reactor heating was switched to propane and the fuel-reactor to methane. The start up burner was switched off, but the air support was still on, to provide oxygen for the methane combustion. After reaching 850 °C all burnable gases have been switched off and another 15 $kg$ of bed material were added. After this interruption heat up continued, burning propane in the air-reactor and methane in the fuel-reactor. When reaching 850 °C again, the fluidization of the loop seals was switched to steam. After reaching the operational temperatures (970 °C in the air-reactor and 900 °C in the fuel-reactor) the air supply in the fuel-reactor was switched off and the system changed into chemical looping mode. In Figure 3.5 the different fluidzation states during start up and operation are shown in pressure profiles of this two states. Fuel-reactor regime seems to be the same like in start up sequence, but the air-reactor profile shows that more material is in the top of the riser during operational conditions than at start up.

### operating point

The average duration for one operating point was 30 minutes. The temperatures in all parts of the rig were stable. Changes in fluidization or other gas streams were avoided, so solids circulation was stable too. The solids sampling (compare 3.4.1) was done at the end of the operating point. When all measurements were done, the next operating point was set and after stabilization of the system parameters the observation started again.

### shut down

First step to start the shut down procedure was to stop the flows of all burnable gases to the system. Additional firing in the air-reactor was stopped. The fuel-reactor was only fluidized with nitrogen at this point. To increase the temperature loss, the cooling jackets on the air-reactor were used. For security reasons the methane support line was flooded with nitrogen, as a consequence also the burner in the fire tube boiler was switched off. After reaching about 600 °C in the bed, the loop seal fluidization was changed from steam to air and the fuel-reactor fluidization from nitrogen to air. At 300 °C all fluidizations were set to minimum

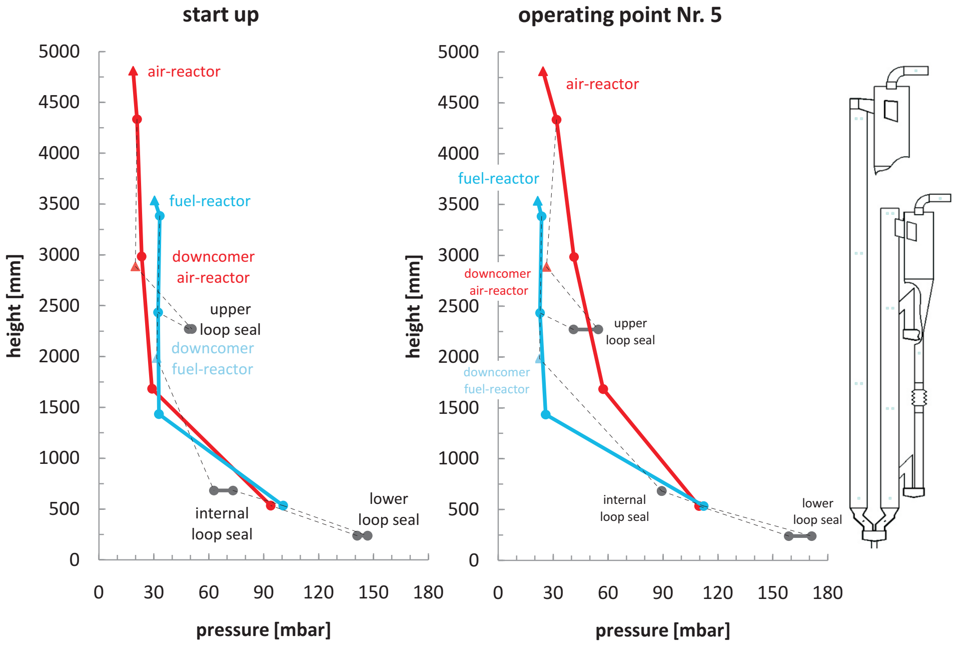

Figure 3.5.: pressure profiles during start up and operating point No. 5 from test run No.7

values and the air support was switched to the local distribution. This mode was hold over night and in the morning of the next day, when the temperature in the bed was about 40 °C, all units were switched off.

## 3.2. Bed materials

The used bed material for the ilmenite tests was provided by Titania A/S (Norway). Normally the material is the basis for $TiO_2$ pigment production, so the claims on purity are high. A chemical composition of he used material is shown in Table 3.2 based on a XRF analysis carried out by Titania A/S. The size distribution of the particles is shown in Figure 3.6. The used olivine was provided by Magnolithe GmbH (Austria). The material is normally used for biomass gasification. The particle size distribution of the olivine was in the same range like the one of the ilmenite material. The nickel enriched olivine had a content of $3.7 wt.\%$ nickel [14]. More information of the nickel enriched olivine can be found in literature [14].

| **species** | **wt.%** |
|---|---|
| $TiO_2$ | 44.08 |
| $Fe^{2+}$ | 25.93 |
| $Fe^{3+}$ | 9.14 |
| $O$ with $Fe$ | 11.36 |
| $P_2O_5$ | 0.03 |
| $S$ | 0.14 |
| $Cr_2O_3$ | 0.08 |
| $SiO_2$ | 3.10 |
| $CaO$ | 0.42 |
| $MgO$ | 4.38 |
| $Al_2O_3$ | 0.93 |
| $MnO$ | 0.29 |
| $K_2O$ | 0.04 |
| $Na_2O$ | 0.10 |
| **Sum** | **100** |

Table 3.2.: chemical composition of the ilmenite used

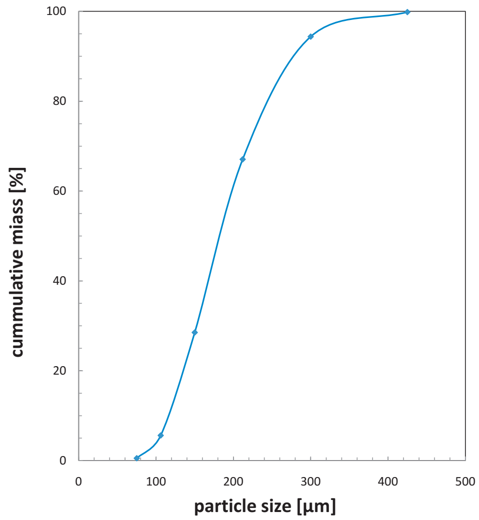

Figure 3.6.: size distribution of the ilmenite used

## 3.3. Analytics

### 3.3.1. Gas analysis

Three gas streams are continuously analysed (compare Figure 3.2). Air-reactor flue gas ($AR_{fg}$), fuel-reactor product gas ($FR_{pg}$) and fire tube boiler off gas ($FTB$). As shown in the flow chart (Figure 3.2) all three sample streams are taken after the heat exchangers. This setup makes it possible to use PTFE tubes for sample gas transport instead of stainless steel tubes. To allow for proper gas analysis the dew point of the gases has to be below 4 °C. To ensure this condition a sample gas preparation station was built. The sample gas streams are transported via heated PTFE tubes to the station. The tubes, which are heated up to 200 °C, guarantee, that the gas temperature is above the dew point when entering the pump in the sample gas preparation unit. First part in in this unit are the heated pumps (compare Figure 3.3.1), for air-reactor flue gas and fire tube boiler off gas KNF Neuberger N 012ST.11e and for the fuel-reactor sample gas KNF Neuberger N 035ST.11e. The sample gas flows are set with needle valves on the inlet side of the pumps. Afterwards the gas streams are cooled down in a condenser, Bühler technologies compressor-sample-gas-condenser EGK 4, to 4 °C. The condensates are collected in three separate vessels. The flows of the dry gases are measured with flow meters, afterwards the streams leave the sample gas preparation unit. The sample gases are transported to the online gas analysers. The air-reactor flue gas is analysed using a Rosemount NGA 2000 ($CO: 0 - 100\%$, $CO_2: 0 - 100\%$,

$O_2 : 0-25\%$), the fuel-reactor product gas is analysed with a Rosemount NGA 2000 ($CO : 0-100\%$, $CO_2 : 0-100\%$, $O_2 : 0-25\%$, $H_2 : 0-100\%$, $CH_4 : 0-100\%$). The indicated values are sent to the computer system, integrated in the visualisation and logged with all data in a file. Due to small diameters in the transport tubes the latency of the gas analysis is very low. During the test runs, gas analysis responded within one minute to changes in the experimental setup.

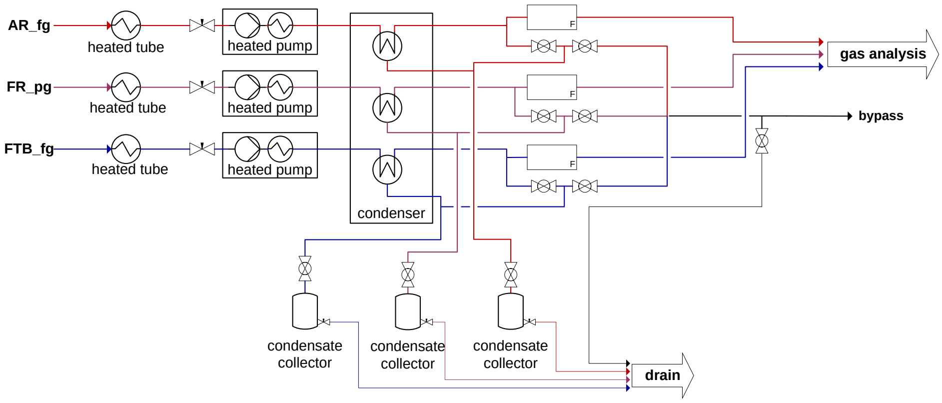

Figure 3.8.: flow chart of the sample gas preparation unit

### 3.3.2. Temperature

Temperature measurement was done at four points in both reactors (compare Figure 3.2). The gas streams to the reactors and also the exhaust streams have their own temperature measurement. The loop seals have thermocouples on their inlet and outlet sides. The measuring points are built of stainless steel pipes which have a threaded connection to the measuring point housing (compare Figure 3.3). In these pipes the thermocouples are installed, the heads are located at the end of the pipe, so insulating effects of the housing are reduced to a minimum. All mounted thermocouples are connected to the PLC, so all measured temperatures are logged and available for data processing. An overview of all measuring points gives Table 3.3.

### 3.3.3. Pressures

Most of the temperature measuring points are also used to measure pressure. In the threaded connection a second pipe is installed and on this pipe a PVC-hose is mounted which leads to the pressure cell. The pressure cells are connected with the PLC, so all measured values are logged. To inhibit hot particles from spitting into the PVC-hose a purge is installed. During start up all measuring points were

| short name | location | short name | location |
|---|---|---|---|
| $TIR\_AR1$ | bottom of AR | $TIR\_LSu\_l$ | loop seal up inlet side |
| $TIR\_AR2$ | after 1/3 of the AR | $TIR\_LSu\_r$ | loop seal up outlet side |
| $TIR\_AR3$ | after 2/3 of the AR | $TIR\_LSl\_l$ | loop seal low inlet side |
| $TIR\_AR4$ | top of the AR | $TIR\_LSl\_r$ | loop seal low outlet side |
| $TIR\_ARfg$ | after the AR cyclone | $TIR\_LSi\_l$ | loop seal internal outlet side |
| $TIR\_DC\_AR$ | in the AR down comer | $TIR\_LSi\_r$ | loop seal internal inlet side |
| $TIR\_FR1$ | bottom of FR | $TIR\_HE\_AR$ | after AR heat exchanger |
| $TIR\_FR2$ | after 1/3 of the FR | $TIR\_HE\_FR$ | after FR heat exchanger |
| $TIR\_FR3$ | after 2/3 of the FR | $TIR\_B\_FR$ | start up burner |
| $TIR\_FR4$ | top of the FR | $TIRC\_AP\_AR\_a1$ | primary air AR after preheater |
| $TIR\_FRpg$ | after the FR cyclone | $TI\_SWITCH\_CASE$ | temperature in the switch case |
| $TIR\_DC\_FR$ | in the FR down comer | $TIRC\_AR\_airt$ | air feed after compressor |
| $TIRC\_AR\_a1$ | primary air before preheater | $TIR\_CP\_Preg$ | natural gas after compressor |
| $TIRC\_CP$ | fuel to fuel-reactor | $TIR\_LSt\_2$ | superheated steam |
| $TI\_FW\_w$ | water feed | $TIR\_FTB$ | fire tube boiler exit |
| $TIR\_BF$ | temperature in the bag filter | $TIR\_ARC1out$ | AR cooling jacket 1 outlet |
| $TIR\_StD$ | temperature in the steam drum | | |

Table 3.3.: overview of temperature measuring points

flooded with a slight air flow of $0.2 - 0.4\ Nl/min$. After switching to CLC mode all measuring points on the fuel reactor side were flooded with argon to prevent a corruption of the gas analysis and the temperature measurement as a consequence of burning the fuel with the air from the scavenging. In Table 3.4 all pressure measuring points are listed and those which are purged with argon are marked.

| short name | Ar | location | short name | Ar | location |
|---|---|---|---|---|---|
| **PIR_ AR1** | | bottom of $AR$ | **PIR_ LSu_ l** | x | loop seal up inlet side |
| **PIR_ AR2** | | after 1/3 of the $AR$ | **PIR_ LSu_ r** | x | loop seal up outlet side |
| **PIR_ AR3** | | after 2/3 of the $AR$ | **PIR_ LSl_ l** | x | loop seal low inlet side |
| **PIR_ AR2** | | top of the $AR$ | **PIR_ LSl_ r** | x | loop seal low outlet side |
| $PIR\_ARfg$ | | after the $AR$ cyclone | **PIR_ LSi_ l** | x | loop seal internal outlet side |
| **PIR_ DC_ AR** | | in the $AR$ down comer | **PIR_ LSi_ r** | x | loop seal internal inlet side |
| **PIR_ FR1** | x | bottom of $FR$ | $PIR\_HE\_AR$ | | after $AR$ heat exchanger |
| **PIR_ FR2** | x | after 1/3 of the $FR$ | $PIR\_HE\_FR$ | | after $FR$ heat exchanger |
| **PIR_ FR3** | x | after 2/3 of the $FR$ | $PIR\_B\_FR$ | | start up burner |
| **PIR_ FR4** | x | top of the $FR$ | $PIRC\_AP\_AR\_a1$ | | primary air $AR$ after preheater |
| $PIR\_FRpg$ | | after the $FR$ cyclone | $PIR\_StD$ | | steam drum |
| **PIR_ DC_ FR** | x | in the $FR$ down comer | $PIRC\_AR\_airt$ | | air feed after compressor |
| $TIRC\_AR\_a1$ | | primary air before preheater | $PIR\_CP\_Preg$ | | pressure after natural gas compressor |
| $PIR\_BF$ | | pressure in the bag filter | $PIRC\_CP$ | | pressure before the natural gas compressor |
| $PDIRC\_BF$ | | pressure drop over the filter bags | $PIR\_FTB$ | | fire tube boiler exit |

Table 3.4.: overview of pressure measuring points, those with scavenging are written in bold letters

## 3.4. Particle analysis

### 3.4.1. Solids sampling

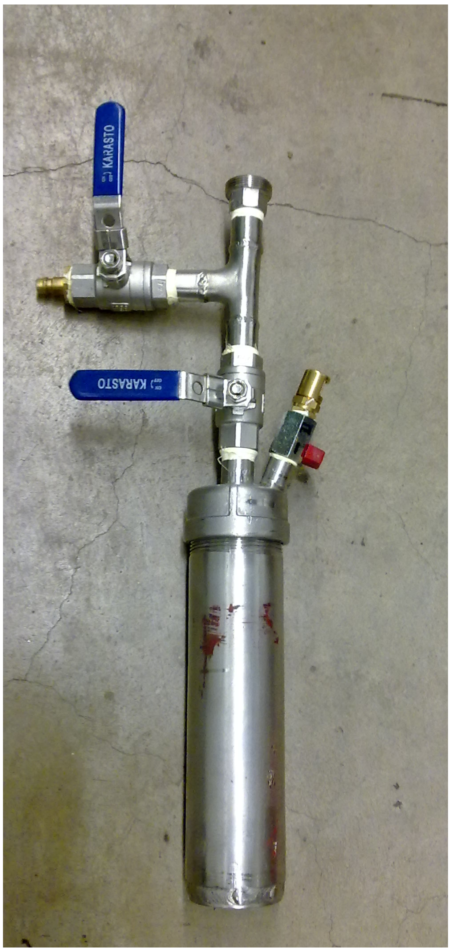

Figure 3.9.: Picture of the solids sampling probe

To obtain solids samples during the test runs under hot conditions a solids sampling probe has been designed and constructed. Figure 3.4.1 shows the unit. The sampling device is mounted in the servicing pipe of the upper loop seal. A temperature resistant pipe ($P-1$ in Figure 3.10) ends directly in the fluidized bed. The pipe is directed downwards to avoid particles rinsing out without the intention of sampling. After the compression type fitting the pipe has a bend and is now vertically oriented. Two ball valves with full bore (valves $V-1$ and $V-2$ in Figure 3.10), to allow unhindered solids flow, and a T-fitting between them are installed. The third connection of the T-fitting is linked with the argon supply over a third ball valve (valve $V-3$ in Figure 3.10). The solids container is connected to this construction. On its top a ball valve (valve $V-4$ in Figure 3.10) is installed, followed by a filter, to avoid blowing out of dust during sampling. The solids container construction is also shown in Figure 3.4.1. The gas solids mixture enters the vessel via a downcomer pipe. This construction alleviates the gas solids separation during the sampling process. To allow easy mounting of the container, a beater is mounted between valve $V-1$ and the T-fitting.
Figure 3.10 shows a flow chart of the solids sampling unit and also the three operational modes of it. If no solids samples are needed, valve $V-1$ will be closed and solids flow in pipe $P-1$ will be inhibited. Before the start of solids sampling, the container should be purged with argon, to avoid reaction of the hot bed material with the oxygen of the air inside. Also pipe $P-1$ should be drained from material, to ensure the accuracy of the solids sample. To do this, at first valves $V-4$ and $V-2$ are opened, then valve $V-3$ is opened too and the container is purged with argon. Afterwards the valves $V-3$ and $V-4$ are closed. To scavenge the sampling pipe, valves $V-1$ and $V-3$ are opened. To start solids sampling, pipe $P-1$ is purged, then valve $V-3$ is closed and simultaneously valve $V-4$ is opened. After collecting enough solids, valve $V-4$ is closed and valve $V-3$ is opened

and particles in the pipe are pushed back into the loop seal. Closing valve $V-1$ disconnects the sampling unit from the reactor system. Opening valves $V-3$ and $V-4$ purges the container with argon. Afterwards all valves are closed and the unit is dismounted. Due to the hot bed material also the container temperature increases, to reduce and avoid reactions of the hot material, the closed container is placed in cold water.

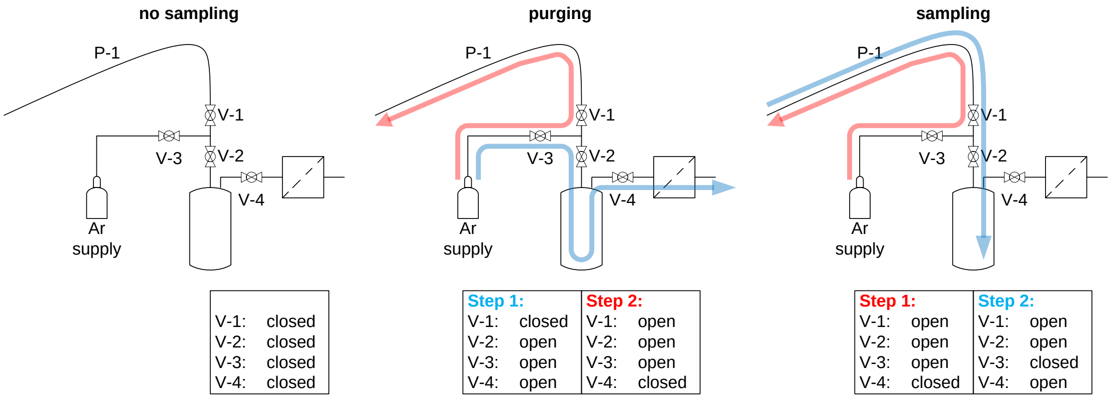

| | |
|---|---|
| V-1: | closed |
| V-2: | closed |
| V-3: | closed |
| V-4: | closed |

| Step 1: | | Step 2: | |
|---|---|---|---|
| V-1: | closed | V-1: | open |
| V-2: | open | V-2: | open |
| V-3: | open | V-3: | open |
| V-4: | open | V-4: | closed |

| Step 1: | | Step 2: | |
|---|---|---|---|
| V-1: | open | V-1: | open |
| V-2: | open | V-2: | open |
| V-3: | open | V-3: | closed |
| V-4: | closed | V-4: | open |

Figure 3.10.: flow chart of the solids sampling

### 3.4.2. X-ray diffraction analysis

X-ray diffraction analysis was carried out on a PANalytical X'pert system. It is used for powder analysis, so the particles had to be crushed before measurement. The X-ray source was a $Cu$-anode and $k\alpha 1$ was 1.5405980Å. The X-ray detector used was a PANalytical X'celerator. The diffractograms were analized with the computer software Maud by Luca Lutterotti [38], which uses the Rietveld algorithm (compare section 2.2.1) for analysis. Figure 3.11 shows the GUI of the software.

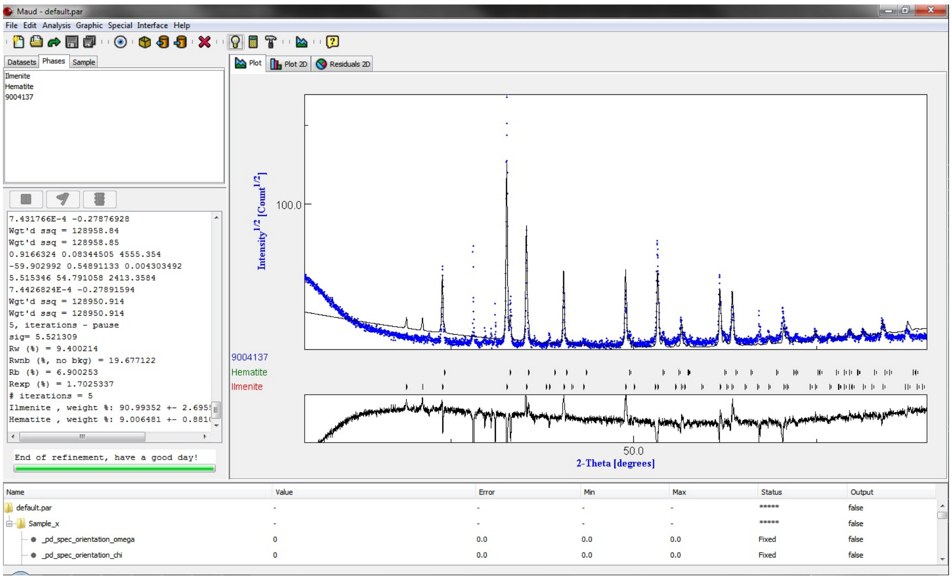

```
7.431766E-4 -0.27876928
Wgt'd ssq = 128958.84
Wgt'd ssq = 128958.85
0.9166324 0.08344505 4555.354
-59.902992 0.54891133 0.004303492
5.515346 54.791058 2413.3584
7.4426824E-4 -0.27891594
Wgt'd ssq = 128950.914
Wgt'd ssq = 128950.914
5, iterations - pause
sig= 5.521309
Rw (%) = 9.400214
Rwnb (%, no bkg) = 19.677122
Rb (%) = 6.900253
Rexp (%) = 1.7025337
# iterations = 5
Ilmenite , weight %: 90.99352 +- 2.695
Hematite , weight %: 9.006481 +- 0.881
```

End of refinement, have a good day!

| Name | Value | Error | Min | Max | Status | Output |
|---|---|---|---|---|---|---|
| default.par | - | - | - | - | ***** | false |
| Sample_x | - | - | - | - | ***** | false |
| _pd_spec_orientation_omega | 0 | 0.0 | 0.0 | 0.0 | Fixed | false |
| _pd_spec_orientation_chi | 0 | 0.0 | 0.0 | 0.0 | Fixed | false |

Figure 3.11.: screen-shot: GUI of the maud-program

### 3.4.3. Thermo gravimetric analysis

The thermogravimetric analysis was carried out on a Netzsch STA 409 (compare Figure 3.12). A ceramic crucible ($Al_2O_3$) was used to carry the samples. The sample mass at the beginnging of the test varied between $0.3[g]$ and $1.1[g]$, the heating rate was $10K/min$ and the operational temperature for the tests was 950°C. With the used test set-up it was possible to heat up under inert, oxidative and reducing conditions. Due to the use of mass flow controllers it was also possible to set precise gas mixtures of reactive gas and inert gas. For oxidation a gas mixture of $20Vol.\%$ oxygen and $80Vol.\%$ nitrogen was used and for reduction, different mixtures of methane and nitrogen in the range of $2.5Vol.\%$ to $33Vol.\%$ were used. The applied solids samples were: fresh, used and definitely oxidised material.

Figure 3.12.: picture of the Netzsch STA 409

## 3.5. Data evaluation

For data evaluation the following parameters and the corresponding formulas should be introduced and described.

### 3.5.1. Methane fuelling

**methane conversion: $X_{CH_4}$**

For operating points, using methane as fuel, the methane conversion is a good parameter to determine the performance of the bed material. It is an indicator for good reactivity towards methane. It is not possible to determine the full carbon conversion with this formula.

$$X_{CH_4} = 1 - \frac{x_{CH_4}}{x_{CH_4} + x_{CO_2} + x_{CO}} \tag{3.1}$$

**carbon dioxide yield: $Y_{CO_2,meth.}$**

The carbon dioxide yield shows the selectivity of the reaction towards $CO_2$. It quantifies the reaction process in the fuel-reactor towards full conversion of the hydrocarbons to carbon dioxide, whereas the methane conversion only represents the reactivity of the solids towards carbon oxidation including also partial oxidation leading to carbon monoxide.

$$Y_{CO_2,meth.} = \frac{x_{CO_2}}{x_{CH_4} + x_{CO_2} + x_{CO}} \tag{3.2}$$

### 3.5.2. Syngas fuelling

**hydrogen conversion: $X_{H_2}$**

When syngas is used as fuel, the hydrogen conversion is an important benchmark for the reactivity of the used bed material. The hydrogen conversion is defined as shown in Equation 3.3.

$$X_{H_2} = \frac{\dot{n}_{H_2,in} - \dot{n}_{H_2,out}}{\dot{n}_{H_2,in}} \tag{3.3}$$

The molar hydrogen flow in the dry fuel-reactor exhaust gas has to be calculated as shown in Equation 3.4, since the normal volume flow is proportional to the molar flow.

$$\dot{n}_{H_2,out} = \frac{x_{H_2}}{x_{CO} + x_{CO_2}} \cdot \dot{n}_{CO,in} \tag{3.4}$$

### carbon monoxide conversion: $X_{CO}$

The second parameter to describe the operating points with syngas fuelling is the carbon monoxide conversion. It reads as shown in Equation 3.5. The carbon monoxide conversion stands for the overall carbon conversion in this operating point.

$$X_{CO} = \frac{x_{CO}}{x_{CO_2} + x_{CO}} \tag{3.5}$$

### carbon dioxide yield: $Y_{CO_2,syng.}$

The carbon dioxide yield calculates as shown in Equation 3.6. Using syngas as fuel, the carbon dioxide yield is not as important as in the methane fuelling case, because it is a function of the carbon monoxide conversion.

$$Y_{CO_2,syng.} = \frac{x_{CO_2}}{x_{CO_2} + x_{CO}} = 1 - X_{CO} \tag{3.6}$$

### 3.5.3. Solids inventory

While operating the rig, it is useful to know the amount of solids in the reactors. To compare different operating points and also different test runs the solids inventory is an important factor to ensure comparability. Using Equation 2.21, it is possible to calculate the height of the fluidized bed. With this height and the diameter of the reactor, the volume of the fluidized bed is accessible. The mass of the bed in the reactor can be calculated as follows.

$$m_{bed} = \rho_b \cdot (r_{reactor}^2 \cdot \pi) \cdot \frac{\Delta P}{(1-\epsilon) \cdot (\rho_p - \rho_g) \cdot g} \tag{3.7}$$

The density of the fluidized bed and also the porosity are not accessible and have to be estimated. It is easier to use the force balance over the fluidized bed. The pressure drop is equivalent to the force directed downwards, so the mass of the bed can be calculated without the estimation of parameters.

$$m_{bed} = \frac{\Delta P \cdot A_{reactor}}{g} \tag{3.8}$$

### 3.5.4. Conversion level of solids

To identify the conversion level of solids during TGA measurements the conversion level [39] is introduced. For the reduction it calculates as shown in Equation 3.9. In the case of oxidation the conversion level can be written as shown in Equation 3.10.

$$X_{s,r} = \frac{m_{ox} - m}{m_{ox} \cdot R_0} \tag{3.9}$$

$$X_{s,o} = 1 - \frac{m_{ox} - m}{m_{ox} \cdot R_0} \tag{3.10}$$

According to Abad [40] the oxygen transport capacity is defined as written in Equation 3.11.

$$R_0 = \frac{m_{ox} - m_{red}}{m_{ox}} \tag{3.11}$$

# 4. Results

## 4.1. Operating parameters

In this work 11 experiments were done, which are described in the listing below (4.1.1). Using methane as fuel, load points in the range of $20kW$ to $120kW$ are possible and stable. When operating with syngas the load range changes to $20kW$ to $100kW$. Stable operating conditions are possible with $70kg$ and also with $85kg$ total solids inventory. The minimization of the mass of total bed inventory has to be investigated in further work.

### 4.1.1. Experiments done

Experiment 1: It was the first hot experiment with ilmenite. It was done to get a sense on the handling of the material. The start up sequence was tested and after reaching the temperature of about 950 °C in the bed the rig was shut down.

Experiment 2: Start up procedure was optimized, propane fuelling in the air-reactor was tested and also the possibility of methane fuelling in the air-reactor. A temperature of about 830 °C in the bed was held for about 90 minutes. Afterwards the system was shut down.

Experiment 3: After start-up procedure the first CLC operating point was set. At about 830 °C air support to the fuel reactor was switched off and chemical looping combustion of methane was started. Temperature was increased slowly to about 970 °C in the air-reactor.

Experiment 4: In this experiment two load points with methane fuelling and one load point with model syngas fuelling were investigated. The total bed inventory was $70kg$ in the beginning, during the experiment the total solids amount was increased to $80kg$

Experiment 5: The focus of this test-run was on the temperature dependency of the process. A temperature-ramp starting at 850 °C to 950 °C was investigated. In the area of increasing temperatures the fuel was hydrogen with nitrogen dilution and with decreasing temperature methane was fuelled.

| **bed material** | **total inventory** | **load** | **fuel** | **temperature** |
|---|---|---|---|---|
| ilmenite | 70kg | 40kW | $CH_4$ | 900 °C |
| ilmenite | 80kg | 30kW | $CO/H_2$ | 900 °C |
| ilmenite | 80kg | 50kW | $CH_4$ | 900 °C |

Table 4.1.: operating points in Experiment 4

Experiment 6: Three types of fuel have been tested in this experiment. The model syngas mixture, pure carbon monoxide and methane as fuel.

| **bed material** | **total inventory** | **load** | **fuel** | **temperature** |
|---|---|---|---|---|
| ilmenite | 70kg | 100kW | $CO/H_2$ 1:1 | 900 °C |
| ilmenite | 70kg | 65kW | $CO/H_2$ 1:1 | 900 °C |
| ilmenite | 70kg | 55kW | $CO/N_2$ 2:1 | 900 °C |
| ilmenite | 70kg | 50kW | $CH_4$ | 900 °C |
| ilmenite | 70kg | 55kW | $CH_4$ | 900 °C |

Table 4.2.: operating points in Experiment 6

Experiment 7: Methane was the only fuel in this experiment. Load variations in the range from $40kW$ to $120kW$ had been done. This variation was done again with 15 additional kilogram of olivine in the bed.

| **bed material** | **total inventory** | **load** | **fuel** | **temperature** |
|---|---|---|---|---|
| ilmenite | 70kg | 40kW | $CH_4$ | 900 °C |
| ilmenite | 70kg | 60kW | $CH_4$ | 900 °C |
| ilmenite | 70kg | 80kW | $CH_4$ | 900 °C |
| ilmenite | 70kg | 100kW | $CH_4$ | 900 °C |
| ilmenite | 70kg | 120kW | $CH_4$ | 900 °C |
| ilmenite/olivine | 70kg + 15kg | 20kW | $CH_4$ | 900 °C |
| ilmenite/olivine | 70kg + 15kg | 40kW | $CH_4$ | 900 °C |
| ilmenite/olivine | 70kg + 15kg | 60kW | $CH_4$ | 900 °C |
| ilmenite/olivine | 70kg + 15kg | 80kW | $CH_4$ | 900 °C |
| ilmenite/olivine | 70kg + 15kg | 100kW | $CH_4$ | 900 °C |
| ilmenite/olivine | 70kg + 15kg | 120kW | $CH_4$ | 900 °C |

Table 4.3.: operating points in Experiment 7

Experiment 8: The program for this experiment was the same like in Experiment 7, but the additional bed material was a nickel-rich-olivine.

| **bed material** | **total inventory** | **load** | **fuel** | **temperature** |
|---|---|---|---|---|
| ilmenite | 70kg | 20kW | $CH_4/N_2$ 1:10 | 900 °C |
| ilmenite | 70kg | 40kW | $CH_4/N_2$ 1:4.5 | 900 °C |
| ilmenite | 70kg | 40kW | $CH_4$ | 900 °C |
| ilmenite | 70kg | 60kW | $CH_4$ | 900 °C |
| ilmenite | 70kg | 80kW | $CH_4$ | 900 °C |
| ilmenite | 70kg | 110kW | $CH_4$ | 900 °C |
| ilmenite/Ni-olivine | 70kg + 15kg | 20kW | $CH_4$ | 900 °C |
| ilmenite/Ni-olivine | 70kg + 15kg | 30kW | $CH_4$ | 900 °C |
| ilmenite/Ni-olivine | 70kg + 15kg | 40kW | $CH_4$ | 900 °C |
| ilmenite/Ni-olivine | 70kg + 15kg | 60kW | $CH_4$ | 900 °C |
| ilmenite/Ni-olivine | 70kg + 15kg | 80kW | $CH_4$ | 900 °C |
| ilmenite/Ni-olivine | 70kg + 15kg | 100kW | $CH_4$ | 900 °C |
| ilmenite/Ni-olivine | 70kg + 15kg | 120kW | $CH_4$ | 900 °C |

Table 4.4.: operating points in Experiment 8

Experiment 9: This experiment had to be stopped after defluidization in the upper loop-seal. After cooling down, agglomerates were found in the upper loop-seal.

Experiment 10: After the crash in Experiment 9, this test run was only for roasting the fresh material. A batch of fresh ilmenite was heated up to 800 °C under oxidising conditions. This state was held for several hours

Experiment 11: In this Experiment 12 different operating points have been investigated. Methane and model syngas were feed gases to the fuel-reactor. The methane load points have been done twice, in the second turn with additional $15kg$ of pre-oxidised ilmenite.

| bed material | total inventory | load | fuel | temperature |
|---|---|---|---|---|
| ilmenite | 70kg | 40kW | $CH_4$ | 900 °C |
| ilmenite | 70kg | 70kW | $CH_4$ | 900 °C |
| ilmenite | 70kg | 80kW | $CH_4$ | 900 °C |
| ilmenite | 70kg | 100kW | $CH_4$ | 900 °C |
| ilmenite | 70kg | 120kW | $CH_4$ | 900 °C |
| ilmenite | 70kg | 45kW | $CO/H_2$ 1:1 | 900 °C |
| ilmenite | 70kg | 80kW | $CO/H_2$ 1:1 | 900 °C |
| ilmenite | 70kg | 100kW | $CO/H_2$ 1:1 | 900 °C |
| ilmenite | 85kg | 40kW | $CH_4$ | 900 °C |
| ilmenite | 85kg | 70kW | $CH_4$ | 900 °C |
| ilmenite | 85kg | 100kW | $CH_4$ | 900 °C |
| ilmenite | 85kg | 120kW | $CH_4$ | 900 °C |

Table 4.5.: operating points in Experiment 11

## 4.2. Active solids-inventory

Using Equation 3.7 leads to the amount of solids in the bed of each reactor. This so-called active-inventory represents the amount of solids which are in contact with the reactive gases. For Experiments 7, 8 and 11 the active-inventory of both reactors and the sum of these, the total active inventory, are shown as a function of fuel power in Figure 4.1.

Along with load variation, also the amount of air fed to the air-reactor changes. Higher global solids circulation causes a shift of inventory from air-reactor to fuel-reactor. The apparent increase of total active inventory with increasing fuel power in the fuel-reactor is wrong since the load variation was done from higher to lower load so the total bed inventory decreased by and by.

Trimming, by increasing the back pressure of the air-reactor exhaust gas stream, effects the inventory of both reactors. Stable operation of the trimmed system was not possible, due to problems with the burner in the fire-tube-boiler. Also the possibility of a leakage in the upper loop-seal, caused from the high pressure in the air-reactor cyclone, is given. The solids inventory in the air-reactor decreases at constant fluidization. This could be the result of bad separation in the cyclones or attrition and a loss of fines in the cyclones. To determine the cause of this effect, the particle loss and the size distribution as a function of experiment duration should be investigated in further work.

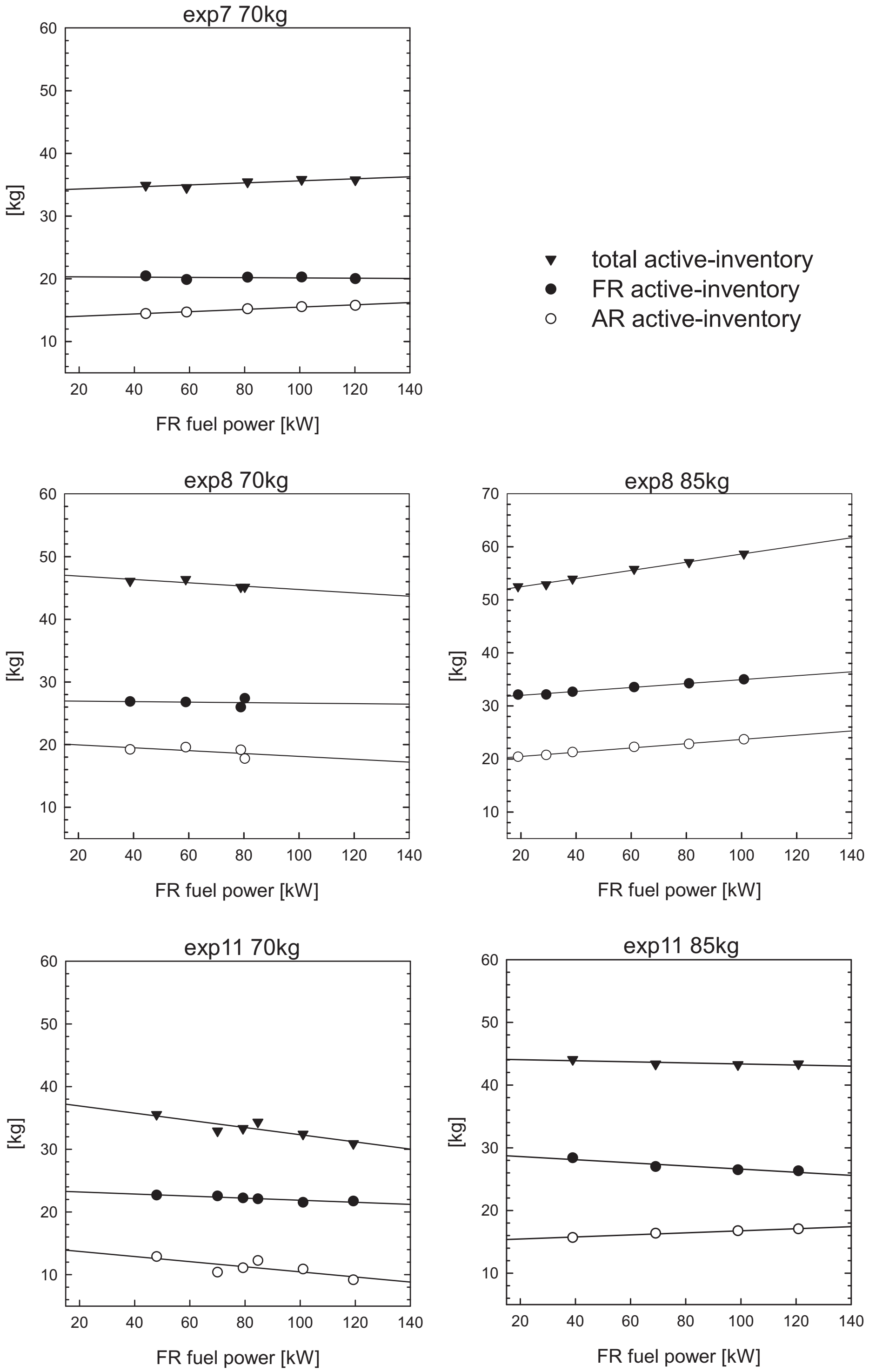

Figure 4.1.: active-inventory of AR and FR as a function of fuel power and total air feed

## 4.3. Conversions

Using Equations 3.1 and 3.2 the results of all experiments with methane fuelling can be drawn as a function of fuel power in the fuel-reactor. These results are shown in Figure 4.3.

Methane conversion decreases with increasing fuel power. Not only the carbon dioxide yield, also the methane conversion gets worse. This behaviour could be a consequence of too little height of the bed. Since fuel-reactor fluidization is a function of the fuel conversion poor reactivity leads to a low expansion of the bed causing too short gas-solids contact-time. This assumption also explains the increase of reactivity when $85kg$ of bed-material were used. These additional $15kg$ of solids were fully added to the total active inventory, because all dead spaces, like the loop-seals, were already filled. The increase of bed-material in the reactor also enhances the height of the bed in the reactor and allows longer gas-solids contact time.

The temperature dependency of the fuel conversion can be shown, using the results of Experiment 5. Figure 4.2 shows the results. Both, hydrogen- and methane-conversion, show a dependency on the average fuel-reactor temperature. Like most oxygen carrier materials, ilmenite performs better at higher temperatures.

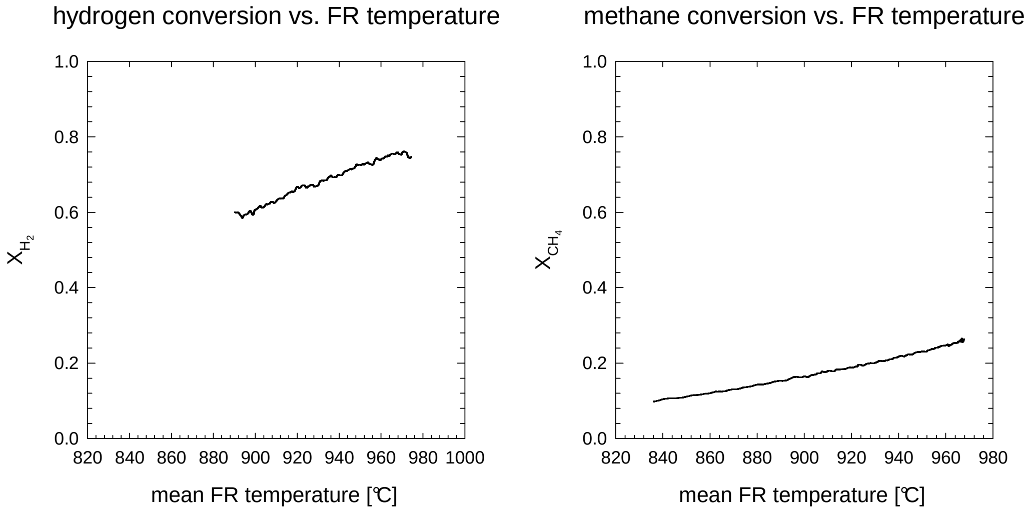

Figure 4.2.: methane conversion and hydrogen conversion as a function of FR - temperature

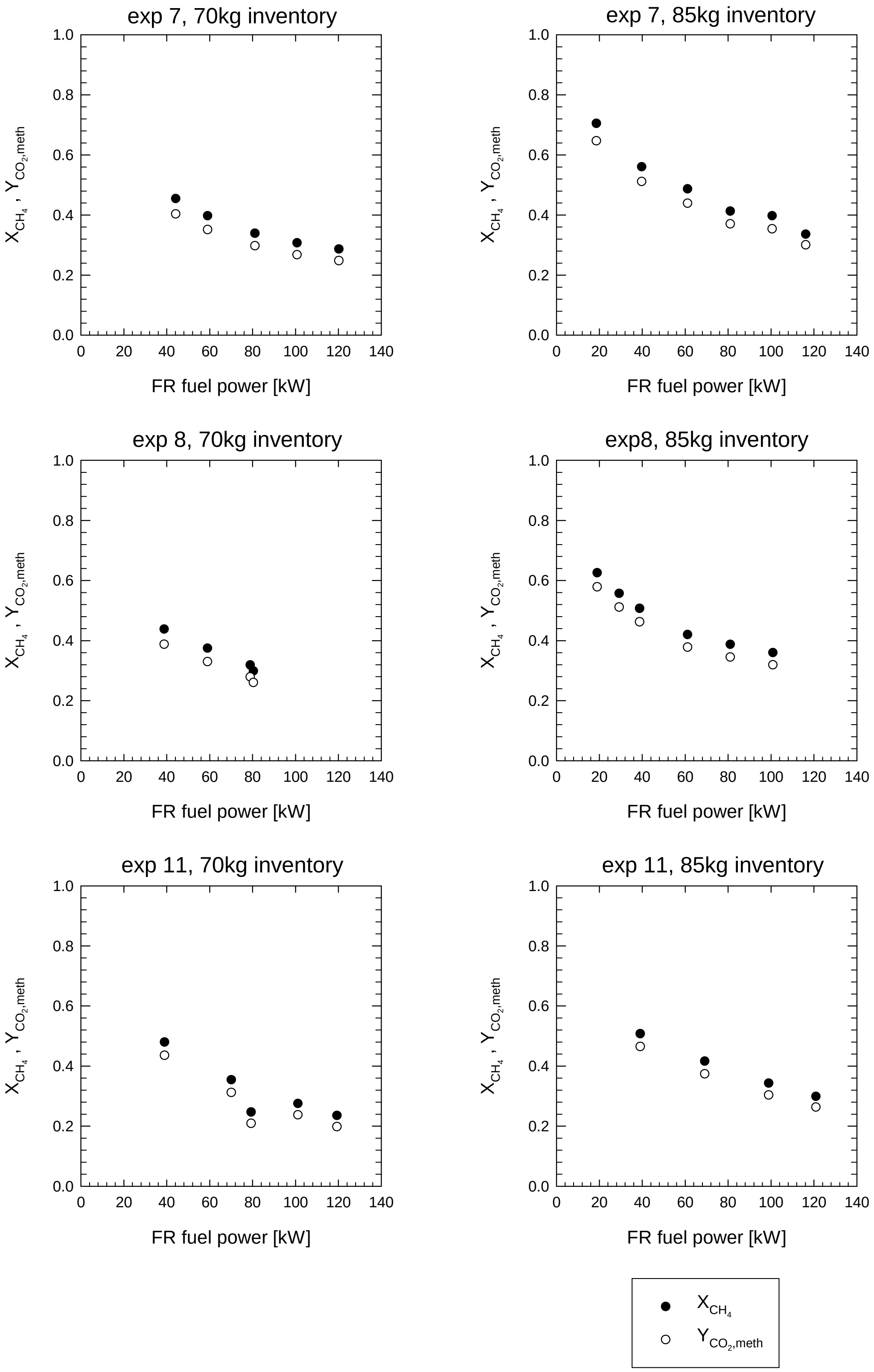

Figure 4.3.: methane conversion and carbon dioxide yield in Experiments 7, 8 and 11 as a function of FR - fuel load

Equations 3.3 and 3.5 give the conversions of hydrogen and carbon-monoxide, when the model syngas is fed to the fuel-reactor. These two values are shown in Figure 4.4 as a function of fuel-power fed to the fuel-reactor.

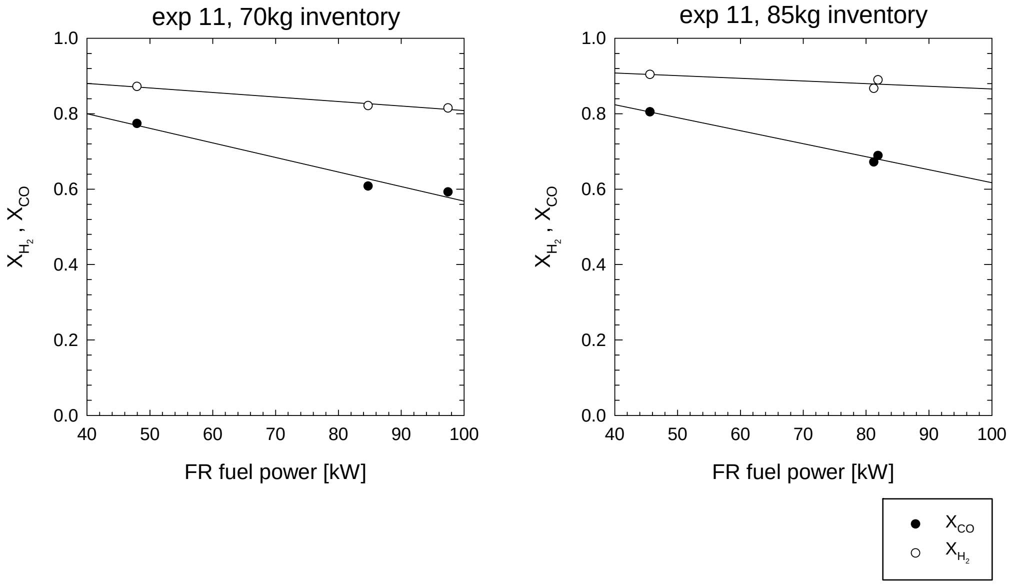

Figure 4.4.: $CO$ and $H_2$ conversions

Both, hydrogen and carbon-monoxide conversion, are better than the conversion of methane. The increase of total solids inventory has a positive effect on the conversion and is in the same range like in the methane fuelling cases. Hydrogen conversion shows less dependency on fuel load compared to carbon-monoxide.

## 4.4. Bedmaterial

Table 4.6 gives an overview of all solids samples taken for X-ray diffraction - and thermo-gravimetric analysis. The samples from the loop seals were taken with the apparatus shown and explained in Section 3.4.1. The samples located in the filter case, have been taken to give information about the abrasion of the particles and the chemical composition of the dust.

TGA-measurements are shown in Figures 4.6 and 4.5. Based on Equations 2.6 3.11 the oxygen transport capacity of ilmenite is:

$$R_0 = 0.05008 \tag{4.1}$$

The reaction rate for reducing the particles shows a big dependency on the content

| **Nr.** | **location** | **date** | **XRD** | **TGA** |
|---|---|---|---|---|
| 1 | filter case | 06.12.2007 | x | |
| 2 | fresh ilmenite | 15.01.2008 | x | x |
| 3 | bed-material sample | 15.01.2008 | x | |
| 4 | LSi | 15.01.2008 | x | |
| 5 | LSl | 06.02.2008 | x | |
| 6 | LSu | 11.02.2008 | x | |
| 7 | LSu | 11.02.2008 | x | |
| 8 | filter case | 18.02.2008 | x | |
| 9 | bed-material sample | 05.03.2008 | x | x |
| 10 | LSu | 06.03.2008 | x | |

Table 4.6.: overview of solids samples for XRD and TGA

of methane in the gas stream. Low concentrations lead to slow reaction. In all cases reduction below $Fe^{2+}$ is possible. The graphs have different endings caused by the different endings of reduction procedure during the measurement. Reaction rates during oxidation are all almost the same, because the the oxygen content and all other conditions were similar in all experiments. But a trend to faster oxidation when older material was used can be recognised. Fresh ilmenite needs a long time to be fully oxidised. This finding fits to the work of Zhang and Ostrovski [22]. Although the material was reduced below $Fe^{2+}$ oxidation shows no change in the rate. Since the samples were in a cubicle during the TGA-measurements without any fluidization the particles stick together. As a consequence for operation in the test rig, ilmenite particles should be fluidized without any disruption.

Figure 4.7 and Table 4.7 show the result of the XRD analysis of sample 1. The detailed results for all samples are reported in the appendix (Tables A.1 to A.11 and Figures A.1 to A.11). Figure 4.8 shows the results of all XRD-analyses to compare the compositions of each sample. Oxidized particles show a high content of pseudobrookite and some rutile and hematite. This result goes along with the results of Sun [41] and Nell [15] and shows that full oxidation of the particles takes place in the air-reactor. The results of Sample 7 have to be investigated further. The missing of rutile in the XRD-analysis of the coarse particles and the presence of this phase in the crushed sample could be an indication of iron enrichment on the surface of the particles. This goes along with the findings of Nell [15] who found iron enrichment on the particle surface during oxidation of ilmenite. To verify this results more samples of uncrushed particles are needed and maybe also some SEM-analysis of the particle surface.

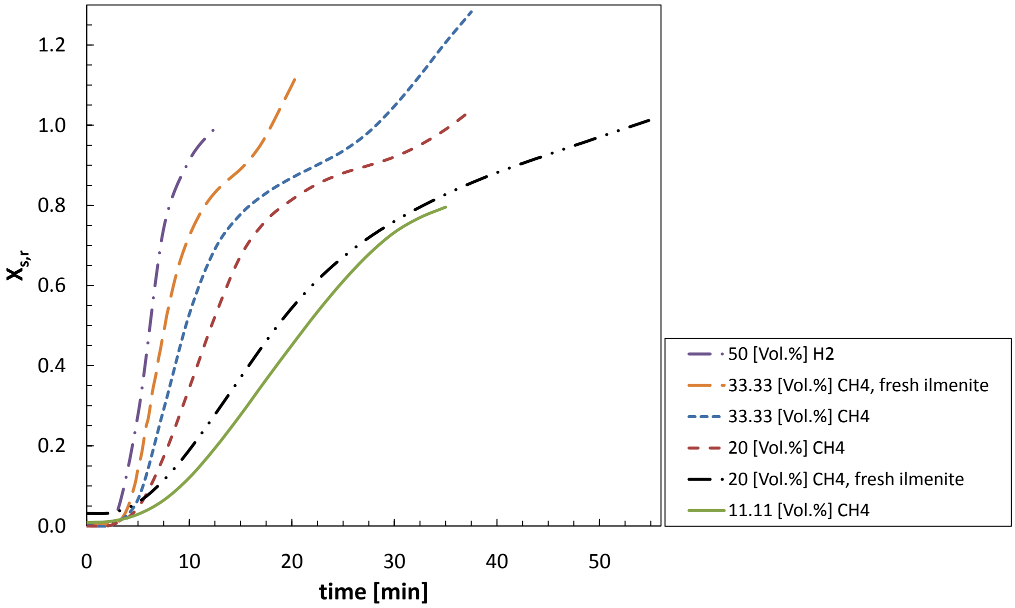

Figure 4.5.: conversion level of reduction during TGA measurements

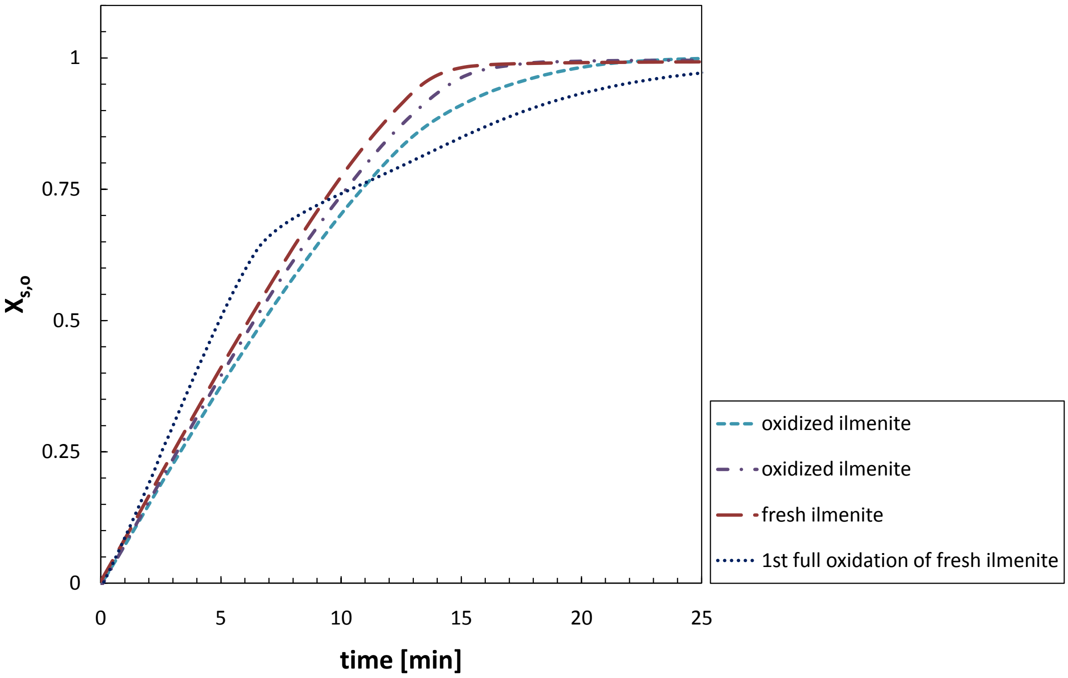

Figure 4.6.: conversion level of oxidation during TGA measurements

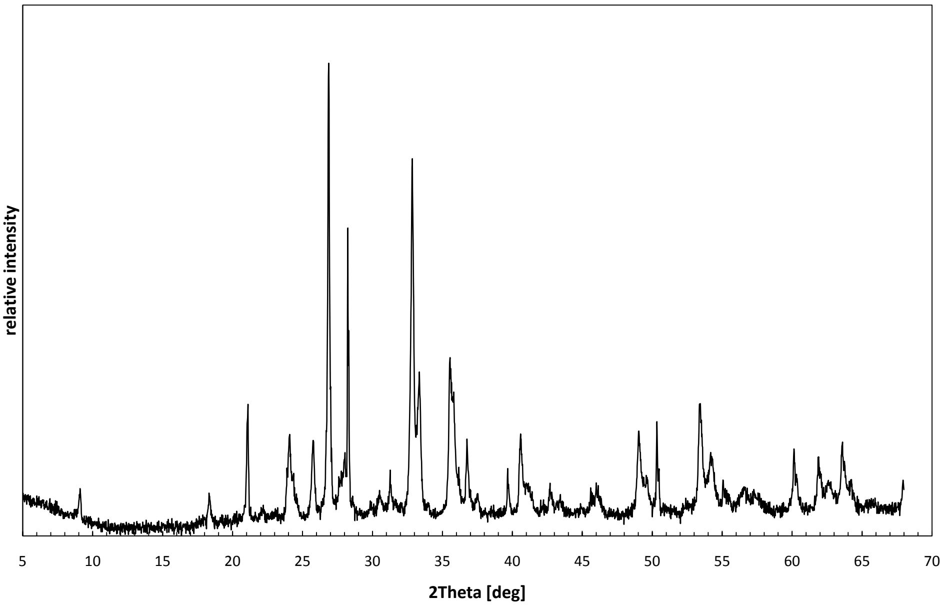

Figure 4.7.: Diffractogram of sample 1 (for diffractograms of other samples see Appendix)

| | $FeTiO_3$ | $TiO_2$ | $MgO$ | Sum |
|---|---|---|---|---|
| [wt%] | 89.4 | 9.5 | 1.1 | 100 |

Table 4.7.: Results of XRD-analysis of sample 1 (for results of other samples see Appendix)

In Figure 4.10 the diffraction patterns of samples 1, 6, 7 and 9 are compared to see how the composition of the material changes with increasing oxidation time. On top, the calculated diffractograms of pure ilmenite, hematite, pseudobrookite and rutile are positioned to identify the corresponding reflexes in the diffraction patterns.

In Figure 4.9 the results of the XRD analyses are plotted in a ternary diagram. Only the Fe, Ti and O containing species are considered and normalized to 1. In the ternary diagram also the calculated composition of the fresh material, based on the XRF - analysis from Titania A/S, are shown. The composition based on the XRF result fits in the alteration of ilmenite. The $TiO_2$ content is stable and only a change in the $FeO$ $Fe_2O_3$ ratio occurs. The XRD analysis of the fresh material shows different results than the calculated composition. At first view it seems that no oxidation took place but the presence of rutile is an indication for oxidation during alteration of the material and leaching of the iron.

The diagram shows the change in phase chemistry during the chemical looping process. The compositions of the oxidized samples are located in the solid solution series of psuedobrookite and ilmenite. The iron content of the oxidized samples is higher than theoretically predicted. This could be an indication of iron enrichment on the surface of the particles. This finding has to be investigated further. Also samples in a reduced state and solids samples after a long term experiment should be analysed to determine attrition and a possible loss of iron as a consequence of iron enrichment on the surface and particle abrasion. Based on the results of this work, ilmenite shows no ageing effects in fuel conversion, nor in attrition.

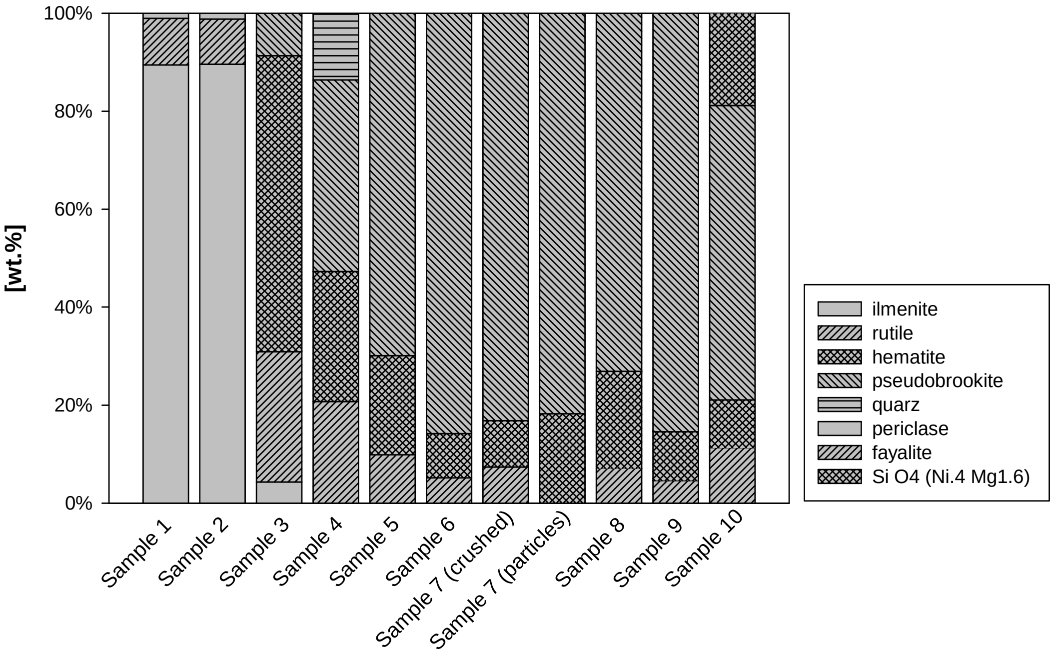

Figure 4.8.: Results of XRD-analysis

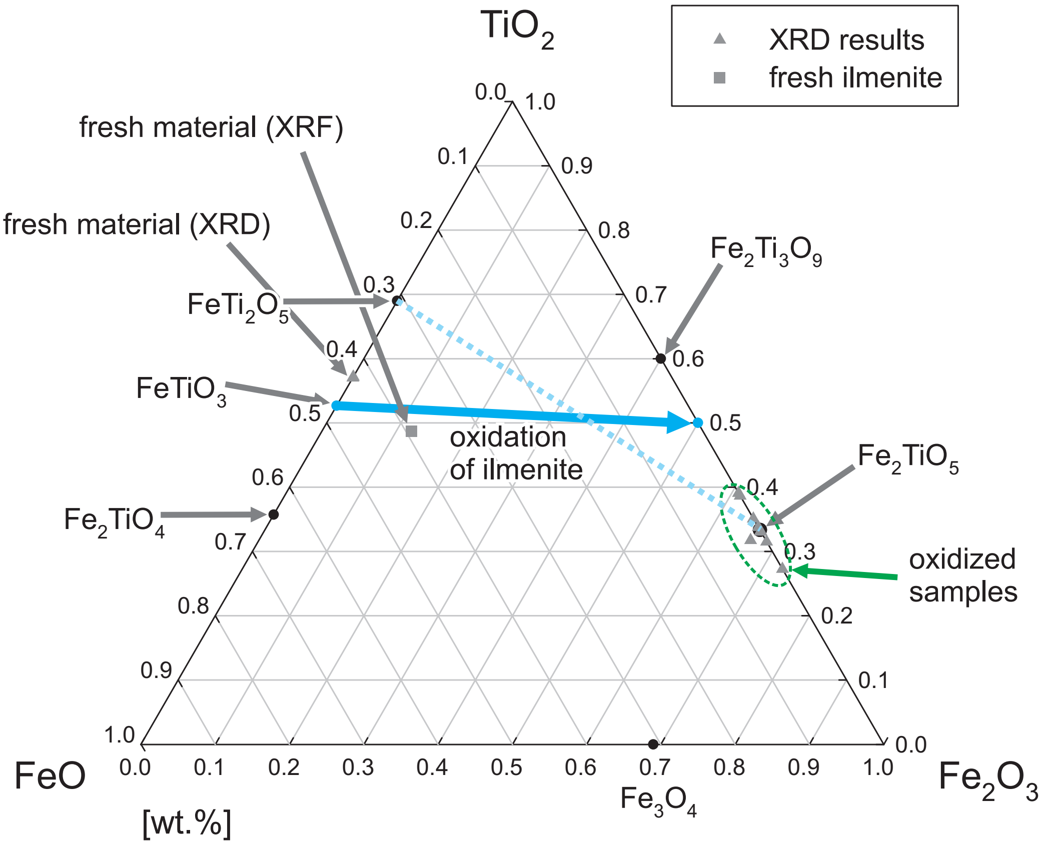

Figure 4.9.: XRD results in a ternary plot for $FeO$, $Fe_2O_3$ and $TiO_2$

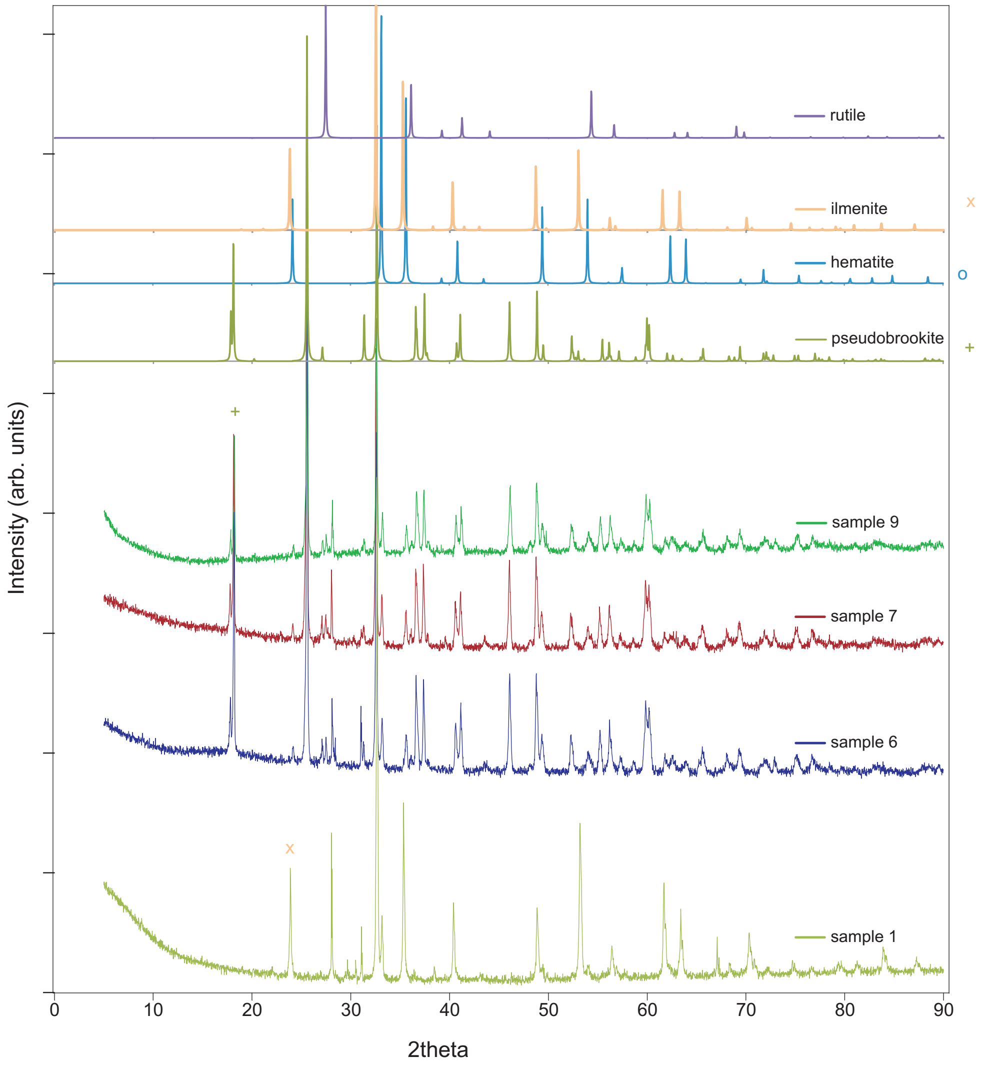

Figure 4.10.: diffractograms of samples 1, 6, 7 and 9

# 5. Conclusions and outlook

According to the results shown in the previous chapter, pure ilmenite is not a good bed material for chemical looping combustion of natural gas feedstock. To burn methane containing gases, other bed materials show much better performance, e.g. Ni-particles. In further work the influence of Ni-additives to ilmenite should be investigated, to improve the methane conversion. Also higher temperatures could lead to better performance of the material.

With carbon monoxide and hydrogen fuelling conversion rates are better. With focus on pure ilmenite as bed material, syngas as fuel should be investigated further.

Olivine does not improve the methane conversion of ilmenite and has no other effect on the product gas composition.

The DCFB reactor system shows high potential for up-scaling to a demo pilot plant, with higher fuel loads. For ilmenite based bed materials a better gas-solid contact in the fuel-reactor should be achieved to improve conversion rates of both fuels, natural gas and syngas.

The bed material sampling system works fine and should be installed in the lower loop seal too, to enable balancing the whole system. It is an easy way to get solids samples from the hot bed during operation.

X-ray diffraction analysis is not the best way to determine the degree of oxidation of the particles. Since the reaction in both reactors takes place on the surface of the particles, the crushing to get a proper diffractogram dilutes the sample with the unreacted core-material. If solids sampling in the lower loop seal is possible, a gravimetric approach to determine the oxidation state of the particles would be a cheap and easy method. The values $X_s, r$ and $X_s, o$ from TG analysis (compare Figures 4.5 and 4.6) describe the state of oxidation of the bed material.

Concluding, the following points should be investigated in further work.

- Optimization of gas-solids contact in the fuel-reactor
- High temperature performance of ilmenite and performance increase with high reactive bed material additives
- Feasibility studies of the potential of integration of chemical looping combustors in existing facilities for heat- and steam-generation

# Nomenclature

| | |
|---|---|
| $(d_p^*)_{AB}$ | dimensionless particle diameter at the A-B boundary ... [-] |
| $(d_p^*)_{BD}$ | dimensionless particle diameter at the B-D boundary ... [-] |
| $(d_p^*)_{CA}$ | dimensionless particle diameter at the C-A boundary ... [-] |
| $\Delta p$ | pressure drop ... [Pa] |
| $\Delta\rho$ | density difference, $\rho_p - \rho_g$ ... $[\nicefrac{kg}{m^3}]$ |
| $\dot{n}_{CO,in}$ | mole flow of carbon monoxide into the fuel-reactor ... $[\nicefrac{mol}{s}]$ |
| $\dot{n}_{H_2,in}$ | mole flow of hydrogen into the fuel-reactor ... $[\nicefrac{mol}{s}]$ |
| $\dot{n}_{H_2,out}$ | mole flow of hydrogen out of the fuel-reactor ... $[\nicefrac{mol}{s}]$ |
| $\dot{Q}$ | gas flow rate ... $[\nicefrac{m^3}{s}]$ |
| $\dot{V}_{or}$ | volume flow through one orifice... $[\nicefrac{cm^3}{s}]$ |
| $\epsilon$ | porosity ... [-] |
| $\epsilon_{mf}$ | porosity at minimum fluidization ... [-] |
| $\lambda$ | wavelength of used x-rays ... $[\AA]$ |
| $\mu$ | dynamic viscosity ... $[\nicefrac{kg}{ms}]$ |
| $\rho_b$ | density of the fluidized bed ... $[\nicefrac{kg}{m^3}]$ |
| $\rho_g$ | gas density ... $[\nicefrac{kg}{m^3}]$ |
| $\rho_p$ | particle density ... $[\nicefrac{kg}{m^3}]$ |
| $\Theta$ | diffraction angle ... $[^\circ]$ |
| $\varphi_p$ | Sphericity of the particle ... [-] |
| $A$ | cross section area of fluidized bed ... $[m^2]$ |
| $A_p$ | cross sectional area of the particle normal to the stream ... $[m^2]$ |
| $Ar$ | archimedes number ... [-] |
| $Ar_{AB}$ | Archimedes number at the A-B boundary ... [-] |

| | |
|---|---|
| $Ar_{BD}$ | Archimedes number at the B-D boundary ... [-] |
| $Ar_{CA}$ | Archimedes number at the C-A boundary ... [-] |
| $C_W$ | drag coefficient ... [-] |
| $D$ | Diameter of the reactor ... [m] |
| $d$ | vertical distance between 2 lattice planes ... $[\mathring{A}\ ]$ |
| $d_{b0}$ | initial bubble size ... [cm] |
| $d_b$ | diameter of a sphere having the same volume as the spherical cap bubble ... [cm] |
| $d_{sv}$ | diameter of a sphere with the same surface/volumina realation like the particle ... [m] |
| $d_s$ | diameter of spherical particle ... [m] |
| $d_t$ | diameter of the fluidized bed ... [cm] |
| $g$ | acceleration of gravity ... $[{}^{m}/{}_{s^2}]$ |
| $H$ | height of the fluidized bed ... $[m]$ |
| $H_{mf}$ | height of the bed at minimum fluidization ... [m] |
| $m$ | mass of the oxygen carrier ... [g] |
| $m_{bed}$ | mass of the fluidized bed ... [kg] |
| $m_{ox}$ | mass of fully oxidised oxygen carrier ... [g] |
| $m_{red}$ | mass of reduced oxygen carrier ... [g] |
| $n$ | diffraction order ... [-] |
| $N'_{or}$ | fictitious number of orifices per area corresponding to touching bubbles ... $[{}^{1}/{}_{cm^2}]$ |
| $N_{or}$ | number of orifices per area... $[{}^{1}/{}_{cm^2}]$ |
| $R_0$ | oxygen transport capacity ... [-] |
| $r_{reactor}$ | inner radius of the reactor ... [m] |
| $Re$ | Reynolds Number ... [-] |
| $Re_c$ | Reynolds number for change from bubbling to turbulent bed ... [-] |
| $Re_{mf}$ | Reynolds number for minimum fluidization ... [-] |

| | |
|---|---|
| $Re_{se}$ | Reynolds number for solids entrainment ... [-] |
| $U$ | superficial velocity ... $[{}^{m}/_{s}]$ |
| $U_{b,ms}$ | lowest bubble rise velocity where slugging occurs ... $[{}^{cm}/_{s}]$ |
| $U_{br}$ | velocity of a single rising bubble ... $[{}^{cm}/_{s}]$ |
| $U_{mb}$ | minimum bubbling velocity ... $[{}^{m}/_{s}]$ |
| $U_{mf}$ | minimum fluidization velocity ... $[{}^{m}/_{s}]$ |
| $U_t$ | terminal velocity ... $[{}^{m}/_{s}]$ |
| $X_{CH_4}$ | methane conversion ... $[-]$ |
| $x_{CH_4}$ | volume fraction of methane in dry exhaust gas... $[vol\%]$ |
| $x_{CO_2}$ | volume fraction of carbon dioxide in dry exhaust gas... $[vol\%]$ |
| $X_{CO}$ | carbon monoxide conversion ... $[-]$ |
| $x_{CO}$ | volume fraction of carbon monoxide in dry exhaust gas... $[vol\%]$ |
| $X_{H_2}$ | hydrogen conversion ... $[-]$ |
| $x_{H_2}$ | volume fraction of hydrogen in dry exhaust gas... $[vol\%]$ |
| $X_{s,o}$ | conversion level under oxidising conditions ... [-] |
| $X_{s,r}$ | conversion level under reducing conditions ... [-] |
| $Y_{CO_2,meth.}$ | carbon dioxide yield with methane fuelling ... $[-]$ |
| $Y_{CO_2,syng.}$ | carbon dioxide yield with syngas fuelling ... $[-]$ |
| $y_{i(calc)}$ | calculated profile at position $2\Theta$ ... [-] |
| $y_{i(obs)}$ | measured profile at position $2\Theta$ ... [-] |
| $z$ | degree of oxidation $(Fe^{3+}/(Fe^{2+}+Fe^{3+})$ ... [-] |
| $z_s$ | limitting bed height to avoid slugging ... [cm] |

# Bibliography

[1] R.K Pachauri and A. Reisinger. Climate change 2007: Synthesis report. *IPCC, Geneva, Switzerland*, Contribution of Working Groups I, II and III to the Fourth Assessment Report of the Intergovernmental Panel on Climate Change, 2007.

[2] D. Solomon, S.and Qin, M. Manning, Z. Chen, M. Marquis, K.B. Averyt, M. Tignor, and Miller H.L. Climate change 2007: The physical science basis. *Cambridge University Press*, Technical Summary, 2007.

[3] OECD/IEA. The role of energy in climate policy. *World Energy Outlook 2008*, 2008.

[4] Ramón Baeza, Balu Balagopal, Eric Boudier, Michael Buffet, and Ingrid Velken. Carbon capture and storage: A solution to the problem of carbon emissions. *The Boston Consulting Group*, 2008.

[5] Alberto Abad, Francisco García-Labiano, Juan Adánez, Luis F. Pilar Gayán de Diego, and Javier Celaya. Applicability limits of cu-, fe-, and ni-based oxygen carriers in chemical - looping combustion. In *8th International Conference on Greenhouse Gas Control Technologies, Trondheim, Norway, 2006*, 2006.

[6] A. Abad, T. Mattisson, A. Lyngfelt, and M. Johansson. The use of iron oxide as oxygen carrier in a chemical-looping reactor. *Fuel*, 86(7-8):1021–1035, 2007.

[7] K.F. Knoche and H. Richter. Verbesserung der reversibilität von verbrennungsprozessen. *Brennstoff-Wärme-Kraft*, 20(5):205–210, 1968.

[8] Beatríz M. Corbella and José María Palacios. Titania-supported iron oxide as oxygen carrier for chemical-looping combustion of methane. *Fuel*, 86(1-2):113–122, 2007.

[9] Masaru Ishida, Hongguang Jin, and Toshihiro Okamoto. A fundamental study of a new kind of medium material for chemical-looping combustion. *Energy & Fuels*, 10:958 – 963, 1996.

[10] Marcus Johansson, Tobias Mattisson, and Anders Lyngfelt. Creating a synergy effect by using mixed oxides of iron- and nickel oxides in the combustion of methane in a chemical-looping combustion reactor. *Energy & Fuels*, 20:2399–2407, 2006.

[11] U.S. Geological Survey. *Mineral commodity summaries 2010.* U.S. Geological Survey, 2010.

[12] Robert T. Downs and Michelle Hall-Wallace. The american mineralogist crystal structure database. *The American Mineralogist*, 88:247–250, 2003.

[13] P. Kolbitsch, T. Pröll, J. Bolhàr-Nordenkampf, and H. Hofbauer. Design of a chemical looping combustor using a dual circulating fluidized bed (dcfb) reactor system. *Chemical Engineering & Technology*, 32(3):398–403, 2009.

[14] Christoph Pfeifer, Rauch Reinhard, and Hofbauer Hermann. In-bed catalytic tar reduction in a dual fluidized bed biomass steam gasifier. *Industrial & Engineering Chemistry Research*, 43:1634–1640, 2004.

[15] J. Nell. An overview of the phase-chemistry involved in the production of high-titanium slag from ilmenite feedstock. *Journal of The South African Institute of Mining and Metallurgy*, 100(1):35–44, 2000.

[16] Joseph Gambogi and S.J. Gerdemann. Titanium metal: Extraction to application. In *A collection of papers from the 1999 TMS Annual Meeting held in San Diego, CA, Feb. 28-Mar. 4, 1999*, pages 175–210. TMS (The Minerals, Metals & Materials Society), Warrendale, PA, 2002.

[17] Ying Chen. Different oxidation reactions of ilmenite induced by high energy ball milling. *Journal of Alloys and Compounds*, 266(1-2):150–154, 1998.

[18] Ying Chen. Low-temperature oxidation of ilmenite (fetio3) induced by high energy ball milling at room temperature. *Journal of Alloys and Compounds*, 257(1-2):156–160, 1997.

[19] Ian E. Grey and Alan F. Reid. The structure of pseudorutile and its role in the natural alteration of ilmenite. *The American Mineralogist*, 60:898–906, 1975.

[20] Kang Sun, Masao Ishiil, Reijiro Takahashi, and Jun-ichiro Yagi. Oxidation kinetics of cement-bonded natural llmenite pellets. *The Iron and Steel Institute of Japan International*, 32(4):489–495, 1992.

[21] Henrik Leion, Anders Lyngfelt, Marcus Johansson, Eric Jerndal, and Tobias Mattisson. The use of ilmenite as an oxygen carrier in chemical-looping combustion. *Chemical Engineering Research and Design*, 3 July 2008 2008.

[22] Guangqing Zhang and Oleg Ostrovski. Effect of preoxidation and sintering on properties of ilmenite concentrates. *International Journal of Mineral Processing*, 64(4):201–218, 2002.

[23] Guanqing Zhang and Oleg Ostrovski. Reduction of titania by methane-hydrogen-argon gas mixture. *Metallurgical and Materials Transactions B*, 31(1):129–139, February 2000.

[24] Kang Sun, Reijiro Takahashi, and Jun-ichiro Yagi. Reduction kinetics of cement-bonded natural llmenite pellets with hydrogen. *The Iron and Steel Institute of Japan International*, 32(4):496–504, 1992.

[25] Kang Sun, Reijiro Takahashi, and Jun-ichiro Yagi. Hydrogen reduction of natural llmenite in a fluidized bed. *The Iron and Steel Institute of Japan International*, 35(4):360–366, 1995.

[26] C.S. Kucukkaragoz and R.H. Eric. Solid state reduction of a natural ilmenite. *Minerals Engineering*, 19:334–337, 2006. Selected papers from Pyrometallurgy '05, Cape Town, South Africa, March 2005.

[27] H.M. Rietveld. A profile refinement method for nuclear and magnetic structures. *Journal of Applied Crystallography*, 2(2):65–71, 1969.

[28] D. Geldart. Types of gas fluidization. *Powder Technology*, 7(5):285–292, 1973.

[29] John R. Grace. Contacting modes and behaviour classification of gas - solid and other two-phase suspensions. *The Canadian Journal of Chemical Engineering*, 64(3):353–363, 1986.

[30] H.T. Bi and J.R. Grace. Flow regime diagrams for gas-solid fluidization and upward transport. *International Journal of Multiphase Flow*, 21(5):1229–1236, 1995.

[31] J.R Grace. Contacing modes and behaviour classification of gas-solid and other twopahse suspensions. *The Canadian Journal of Chemical Engineering*, (64):353–363, 1986.

[32] D. Geldart and A.R. Abrahamsen. Homogeneous fluidization of fine powders using various gases and pressures. *Powder Technology*, 19(1):133 – 136, 1978.

[33] Daizo Kunii and Octave Levenspiel. *Fluidization Engineering*. Butterworth - Heinemann, second edition, 1991.

[34] Carl Linderholm, Tobias Mattisson, and Anders Lyngfelt. Long-term integrity testing of spray-dried particles in a 10-kW chemical-looping combustor using natural gas as fuel. *Fuel*, (88):2083–2096, 12.01.2009 2009.

[35] Tobias Pröll, Philipp Kolbitsch, Johannes Bolhàr-Nordenkampf, and Hermann Hofbauer. A novel dual circulating fluidized bed system for chemical looping processes. *AIChE Journal*, 55(12):3255–3266, 2009.

[36] J.R. Grace, A.A. Avidan, and T.M. Knowlton. *Circulating Fluidized Beds*. Blackie Academic & Professional, 1 edition, 1997.

[37] E. Hugi. Auslegung hochbeladener zyklonabscheider für zirkulierende gas/feststoff-wirbelschicht-reaktorsysteme. Technical report, 1997.

[38] Ischia G. Lonardelli I. Wenk H.-R. Lutterotti L., Bortolotti M. Rietveld texture analysis from diffraction images. *Zeitschrift für Kristallographie Supplements*, 26:125 – 130, 2007.

[39] F. Garcia-Labiano, L.F. de Diego, J. Adánez, A. Abad, and P. Gayán. Reduction and oxidation kinetics of a copper-based oxygen carrier prepared by impregnation for chemical-looping combustion. *Industrial & Engineering Chemistry Research*, 43(26):8168–8177, 2004.

[40] Alberto Abad, Francisco Garciá-Labiano, Luis F. de Diego, Pilar Gayán, and Juan Adánez. Reduction kinetics of cu-, ni-, and fe-based oxygen carriers using syngas (co + h2) for chemical-looping combustion. *Energy & Fuels*, 21:1843–1853, 2007.

[41] Kang Sun, Reijiro Takahashi, and Jun-ichiro Yagi. Kinetics of the oxidation and reduction of synthetic llmenite. *The Iron and Steel Institute of Japan International*, 33(5):523–528, 1993.

# List of Figures

# List of Tables

# A. Diffractograms

## Sample1

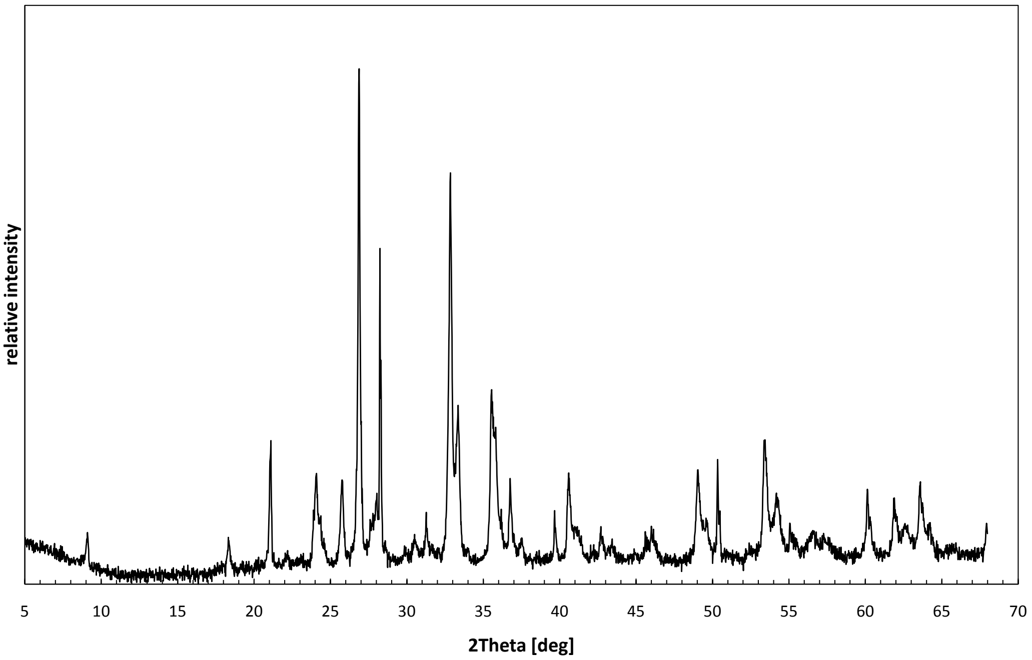

Figure A.1.: diffractogram of sample 1

| | $FeTiO_3$ | $TiO_2$ | $MgO$ | Sum |
|---|---|---|---|---|
| [wt%] | 89.4 | 9.5 | 1.1 | 100 |

Table A.1.: results of XRD-analysis of sample 1

## Sample2

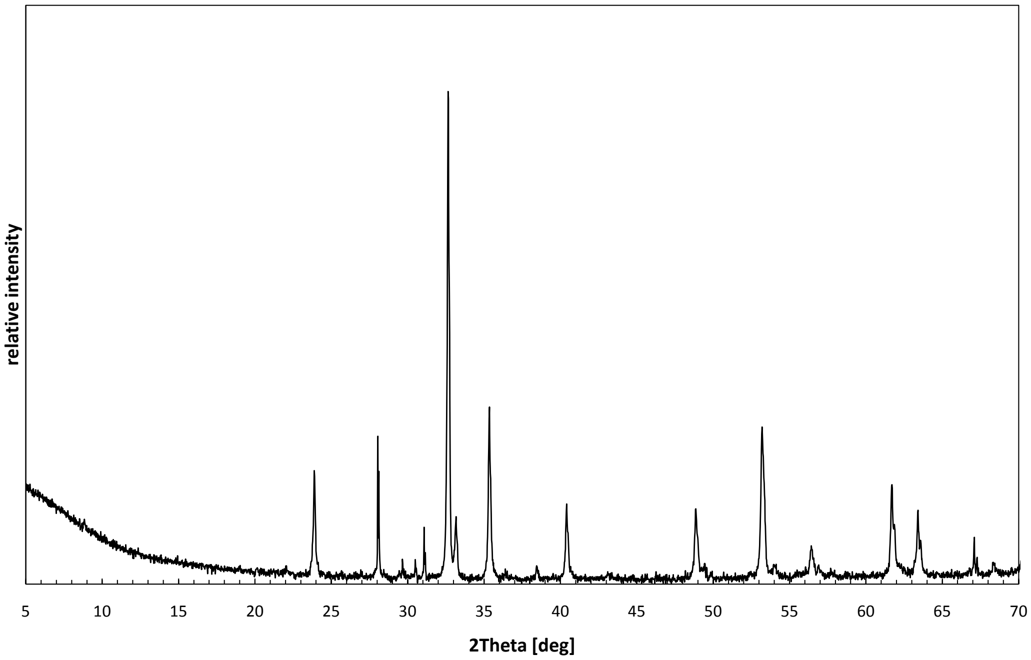

Figure A.2.: diffractogram of sample 2

| | $FeTiO_3$ | $TiO_2$ | $MgO$ | Sum |
|---|---|---|---|---|
| [wt%] | 89.6 | 9.2 | 1.2 | 100 |

Table A.2.: results of XRD-analysis of sample 2

## Sample3

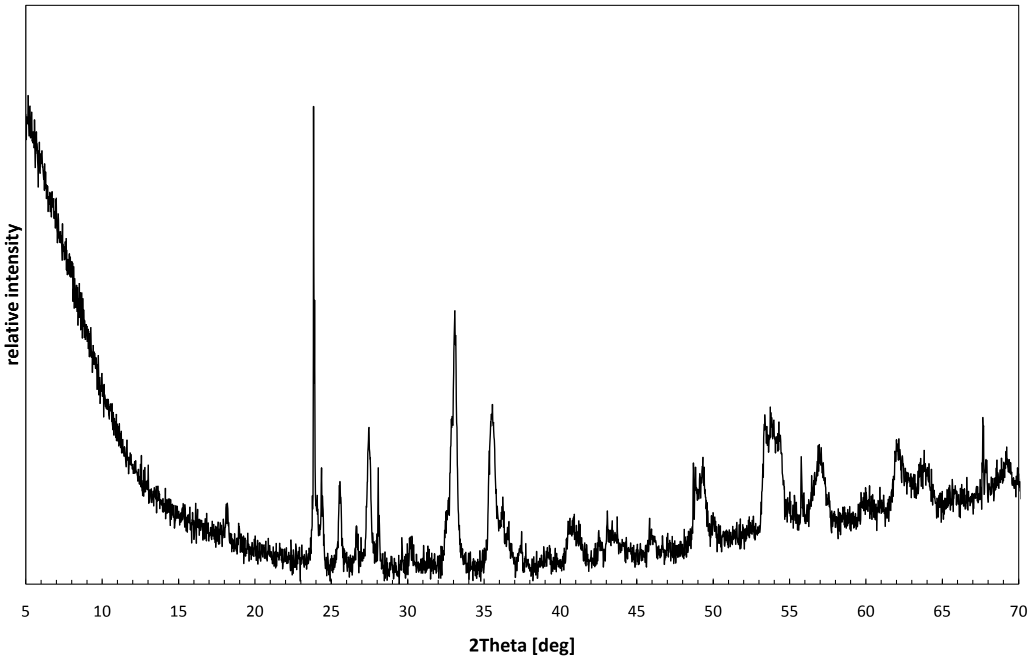

Figure A.3.: diffractogram of sample 3

| | $FeTiO_3$ | $TiO_2$ | $Fe_2O_3$ | Sum |
|---|---|---|---|---|
| [wt%] | 89.4 | 9.5 | 1.1 | 100 |

Table A.3.: results of XRD-analysis of sample 3

## Sample4

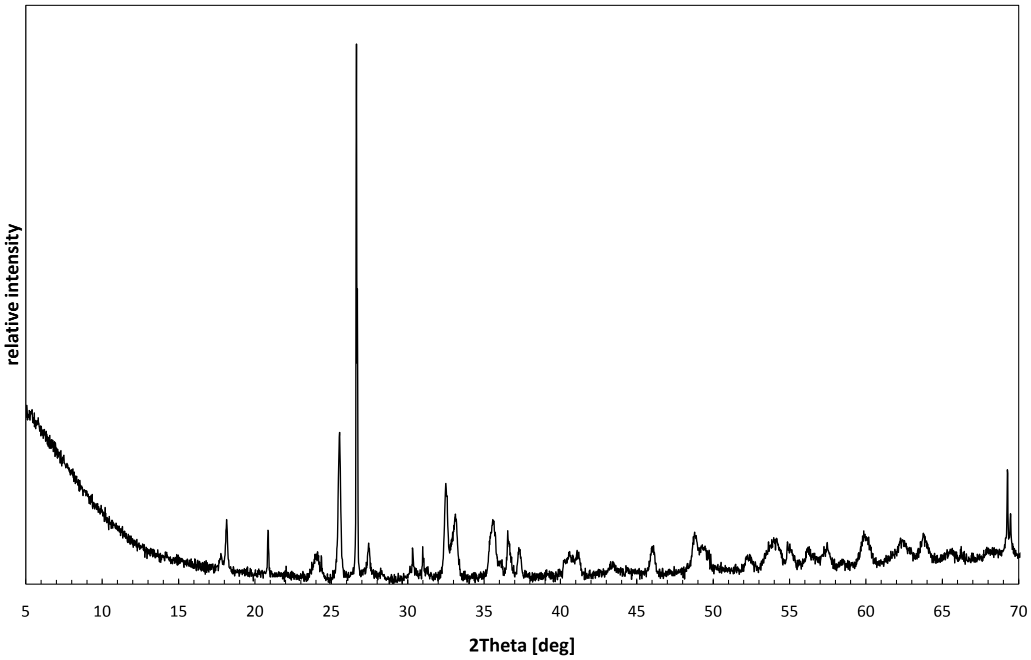

Figure A.4.: diffractogram of sample 4

| | $TiO_2$ | $Fe_2O_3$ | $Fe_2TiO_5$ | $SiO_2$ | Sum |
|---|---|---|---|---|---|
| [wt%] | 20.7 | 26.5 | 39.1 | 13.6 | 100 |

Table A.4.: results of XRD-analysis of sample 4

## **Sample5**

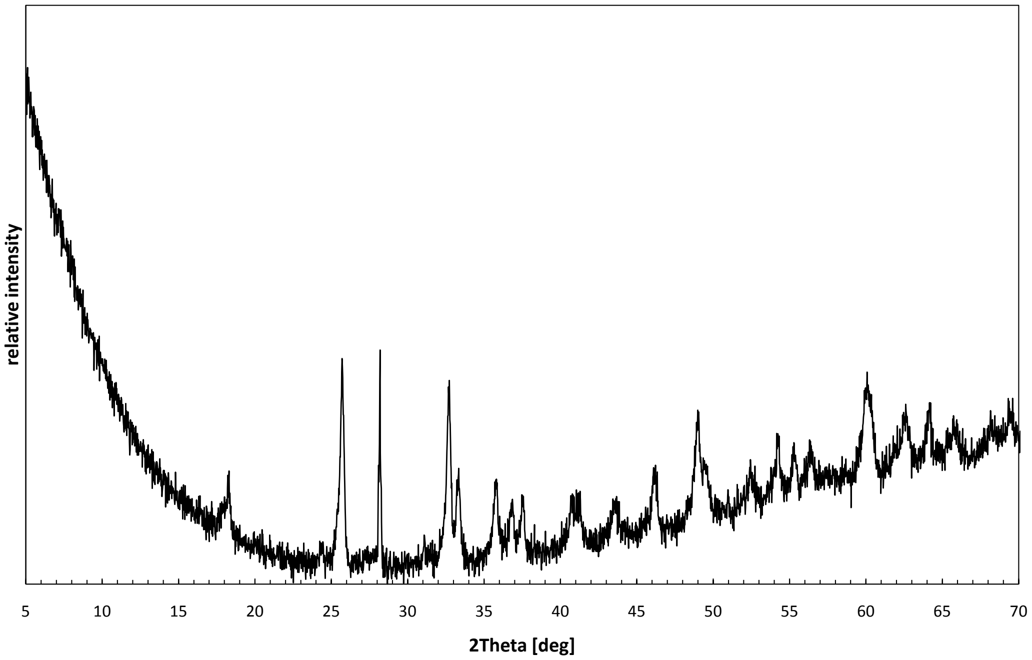

Figure A.5.: diffractogram of sample 5

| | $TiO_2$ | $Fe_2O_3$ | $Fe_2TiO_5$ | Sum |
|---|---|---|---|---|
| [wt%] | 9.9 | 20.2 | 69.9 | 100 |

Table A.5.: results of XRD-analysis of sample 5

## Sample6

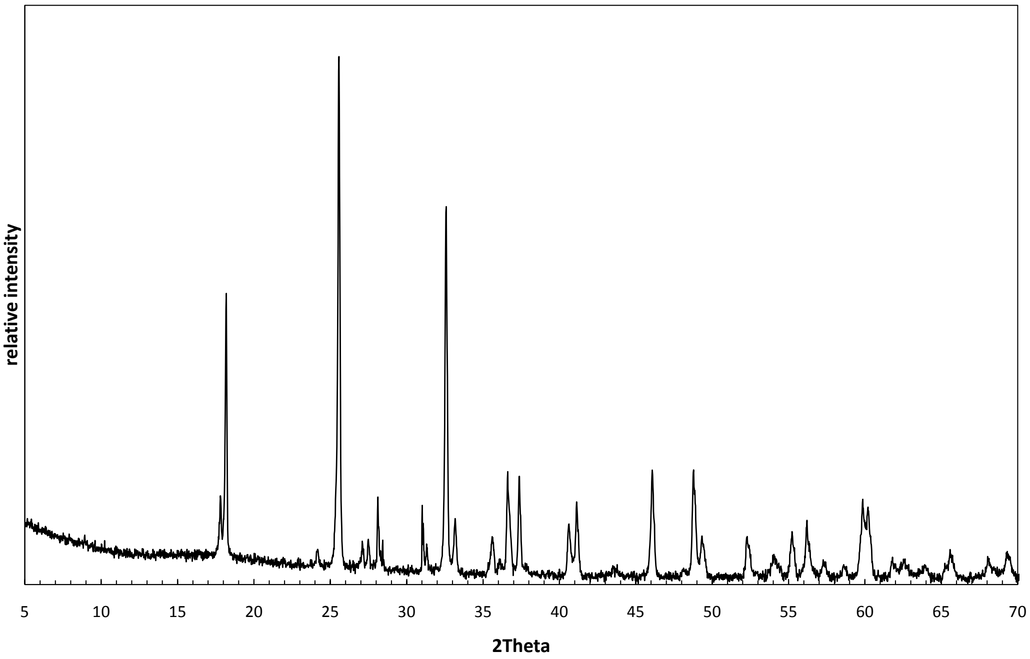

Figure A.6.: diffractogram of sample 6

| | $TiO_2$ | $Fe_2O_3$ | $Fe_2TiO_5$ | Sum |
|---|---|---|---|---|
| [wt%] | 5.2 | 9.0 | 85.8 | 100 |

Table A.6.: results of XRD-analysis of sample 6

## Sample7 (crushed particles)

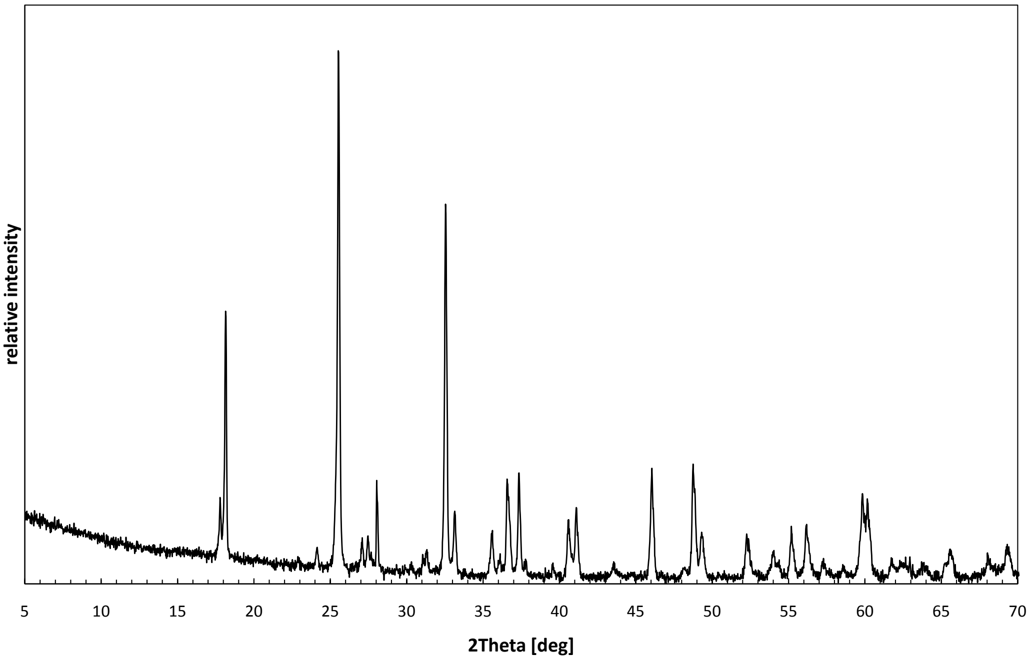

Figure A.7.: diffractogram of sample 7 (crushed particles)

| | $TiO_2$ | $Fe_2O_3$ | $Fe_2TiO_5$ | Sum |
|---|---|---|---|---|
| [wt%] | 7.3 | 9.4 | 83.2 | 100 |

Table A.7.: results of XRD-analysis of sample 7 (crushed particles)

## Sample7 (whole particles)

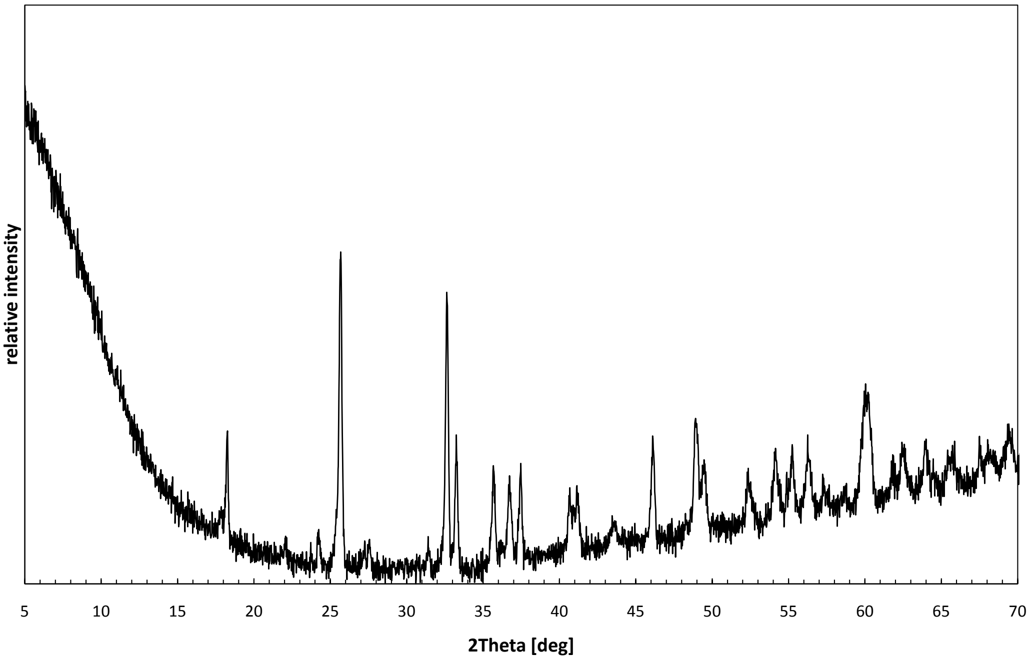

Figure A.8.: diffractogram of sample 7 (whole particles)

| | $Fe_2O_3$ | $Fe_2TiO_5$ | Sum |
|---|---|---|---|
| [wt%] | 18.2 | 81.8 | 100 |

Table A.8.: results of XRD-analysis of sample 7 (whole particles)

## Sample8

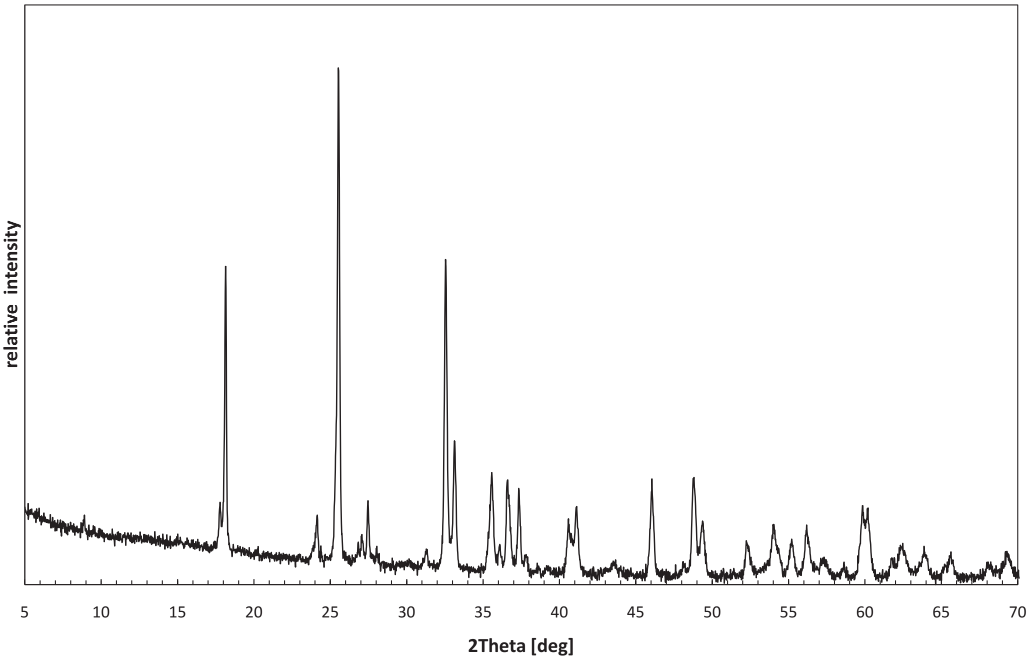

Figure A.9.: diffractogram of sample 8

| | $TiO_2$ | $Fe_2O_3$ | $Fe_2TiO_5$ | Sum |
|---|---|---|---|---|
| [wt%] | 7.1 | 19.7 | 73.1 | 100 |

Table A.9.: results of XRD-analysis of sample 8

## Sample9

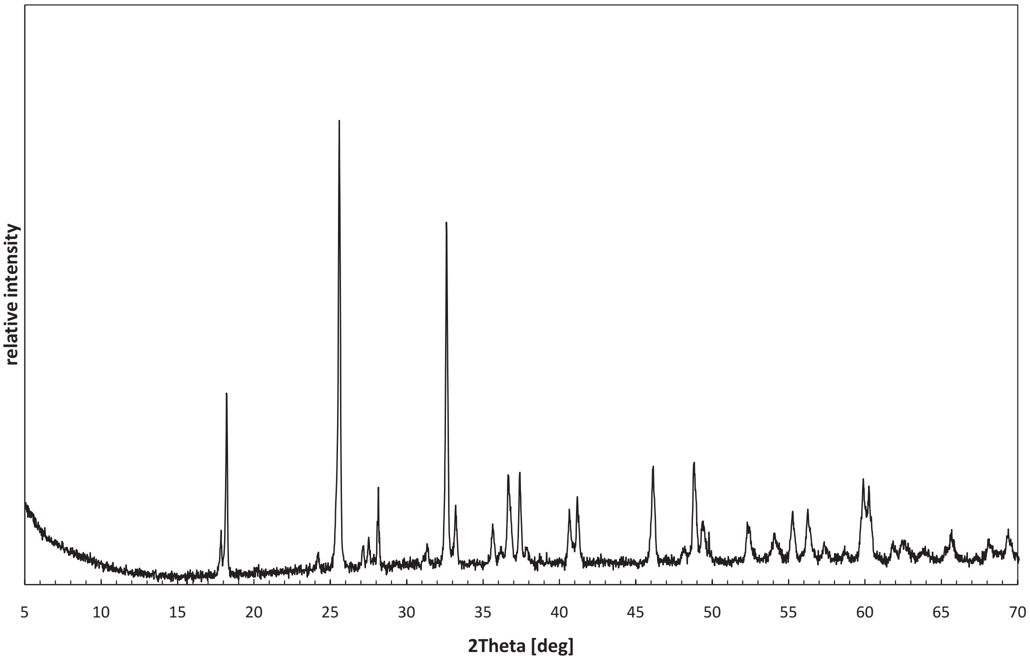

Figure A.10.: diffractogram of sample 9

| | $TiO_2$ | $Fe_2O_3$ | $Fe_2TiO_5$ | Sum |
|---|---|---|---|---|
| [wt%] | 4.6 | 10.0 | 85.4 | 100 |

Table A.10.: results of XRD-analysis of sample 9

## Sample10

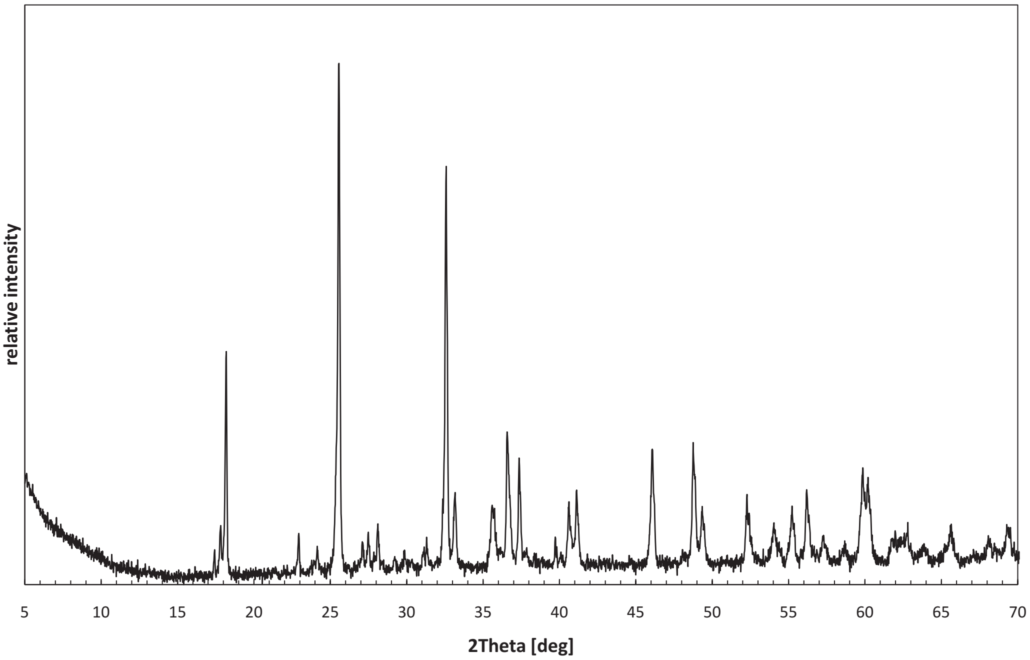

Figure A.11.: diffractogram of sample 10

| | $TiO_2$ | $Fe_2O_3$ | $Fe_2TiO_5$ | $SiO_4(Ni_{0.4}Mg_{1.6})$ | Sum |
|---|---|---|---|---|---|
| [wt%] | 11.3 | 9.8 | 60.1 | 18.8 | 100 |

Table A.11.: results of XRD-analysis of sample 10